

SOLVING ATOMIC STRUCTURE USING STATISTICAL MECHANICAL SEARCHES ON  
X-RAY SCATTERING DERIVED POTENTIAL ENERGY SURFACES

by

Christopher James Wright

Bachelor of Science  
Brown University 2014

---

Submitted in Partial Fulfillment of the Requirements

for the Degree of Masters of Science in

Chemical Engineering

College of Engineering and Computing

University of South Carolina

2016

Accepted by:

Xiao-Dong Zhou, Major Professor

Thomas Vogt, Committee Member

Mark Uline, Committee Member

Jochen Lauterbach, Committee Member

Lacy Ford, Vice Provost and Dean of Graduate Studies

© Copyright by Christopher James Wright, 2016  
All Rights Reserved.

## DEDICATION

## ACKNOWLEDGMENTS

## ABSTRACT

## TABLE OF CONTENTS

DEDICATION . . . . .	iii
ACKNOWLEDGMENTS . . . . .	iv
ABSTRACT . . . . .	v
LIST OF TABLES . . . . .	ix
LIST OF FIGURES . . . . .	x
TODO LIST . . . . .	1
CHAPTER 1 STATISTICAL MECHANICAL ENSEMBLES AND POTENTIAL ENERGY SURFACES . . . . .	5
1.1 Introduction . . . . .	5
1.2 Potential Energy Surfaces . . . . .	5
1.3 Ensembles . . . . .	7
CHAPTER 2 ATOMIC PAIR DISTRIBUTION FUNCTION: THEORY AND COMPUTATION . . . . .	12
2.1 Theory . . . . .	12
2.2 Computation . . . . .	14
CHAPTER 3 BENCHMARKING . . . . .	18

3.1 PDF . . . . .	18
3.2 PDF with ADPs . . . . .	18
CHAPTER 4 X-RAY TOTAL SCATTERING DATA ACQUISITION AND PROCESSING . . . . .	24
4.1 Experiment . . . . .	24
4.2 Data Processing Workflow . . . . .	24
CHAPTER 5 ANNEALING AND AGGREGATION OF 2NM AU NANOPARTICLES . . . . .	41
5.1 Experiments . . . . .	41
5.2 Data Processing . . . . .	41
5.3 Data Analysis . . . . .	41
5.4 Simulation . . . . .	41
5.5 Structural Analysis . . . . .	41
5.6 Conclusions . . . . .	41
CHAPTER 6 PHASE CHANGES AND ANNEALING DYNAMICS OF $\text{Pr}_2\text{NiO}_4$ AND ITS DERIVATIVES . . . . .	42
6.1 Experiments . . . . .	42
6.2 Data Processing . . . . .	42
6.3 Data Analysis . . . . .	42
6.4 Simulation . . . . .	42
6.5 Structural Analysis . . . . .	42
6.6 Conclusions . . . . .	42

CHAPTER 7 CONCLUSION . . . . .	43
--------------------------------	----

## LIST OF TABLES

## LIST OF FIGURES

Figure 2.1 Comparison of the CPU and GPU chip architectures . . . . .	15
Figure 3.1 Au <sub>55</sub> PDF fitting of DFT-optimized <i>c</i> -Au <sub>55</sub> . a) the final structural solution ( $Rw=0.3\%$ ) with bond lengths color-coded by step of 0.05Å, b) the target PDF(blue dots) overlaid with the PDF of the final structure (solid red lines) with the difference in green lines offset below, c) the radial bond distribution, and d) bond angle distribution. . . . .	19
Figure 3.2 Au <sub>55</sub> PDF fitting of surface-disordered Au <sub>55</sub> . a) the target structure, b) the final structural solution ( $Rw=0.6\%$ ), c) the comparison of PDFs, d) the CN distribution with the number of atoms in either the core or the surface, e) the radial bond distribution, and f) the bond angle distribution. . . . .	20
Figure 3.3 Similar to figure 3.2 for DFT-optimized amorphous Au <sub>55</sub> . . . . .	21
Figure 3.4 Similar to figure 3.2 for Au <sub>102</sub> as in DFT-optimized Au <sub>102</sub> MBA <sub>44</sub> cluster. . . . .	22
Figure 3.5 Similar to Fig. 3.4 with Marks decahedron as the starting structure. . . . .	23
Figure 4.1 Database Loading Workflow. Data is loaded from various sources, including images and text files, into the FileStore and Meta-dataStore databases. Data is then retrieved from the databases using the databroker. . . . .	25
Figure 4.2 Scattering onto a flat detector . . . . .	26
Figure 4.3 $Q$ resolution as a function of $Q$ . . . . .	27
Figure 4.4 Number of pixels as a function of $Q$ , binned at the $Q$ resolution of the detector. . . . .	28

Figure 4.5 Generated dead/hot pixel masks for a detector with 100 bad pixels. a) the standard even bin mask and b) the $Q$ resolution binned mask. The bad pixels are noted with open circles, masked pixels are noted with closed circles. . . . .	30
Figure 4.6 Generated dead/hot pixel masks for a detector with 300 bad pixels. a) the standard even bin mask and b) the $Q$ resolution binned mask. The bad pixels are noted with open circles, masked pixels are noted with closed circles. . . . .	30
Figure 4.7 Generated dead/hot pixel masks for a detector with 500 bad pixels. a) the standard even bin mask and b) the $Q$ resolution binned mask. The bad pixels are noted with open circles, masked pixels are noted with closed circles. . . . .	31
Figure 4.8 Generated dead/hot pixel masks for a detector with 1000 bad pixels. a) the standard even bin mask and b) the $Q$ resolution binned mask. The bad pixels are noted with open circles, masked pixels are noted with closed circles. . . . .	31
Figure 4.9 Generated beamstop holder masks for a beamstop holder with 10% transmittance. a) the raw image, b) the masked image, c) and the missed pixels . . . . .	32
Figure 4.10 Generated beamstop holder masks for a beamstop holder with 30% transmittance. a) the raw image, b) the masked image, c) and the missed pixels . . . . .	32
Figure 4.11 Generated beamstop holder masks for a beamstop holder with 50% transmittance. a) the raw image, b) the masked image, c) and the missed pixels . . . . .	32
Figure 4.12 Generated beamstop holder masks for a beamstop holder with 90% transmittance. a) the raw image, b) the masked image, c) and the missed pixels . . . . .	33
Figure 4.13 Generated beamstop holder masks which is rotated away from verticle . . . . .	33
Figure 4.14 Masked experimental data. a) the raw image, b) the mask . . . . .	34
Figure 4.15 Masked experimental data with Pt single crystal signal. a) the raw image, b) the mask . . . . .	34

Figure 4.16 Masked experimental data with Pt single crystal signal using figure's 4.14 as a starting mask. a) the raw image, b) the mask . . . . . 35

Figure 4.17 Masking, average, and standard deviation of an example x-ray total scattering measurement. This image was produced with no mask. a) the image, b) the mask, c) the mean and median values, d) the standard deviation (normalized to the median), e) a closeup of the  $28 \text{ \AA}^{-1}$ to  $31 \text{ \AA}^{-1}Q$  range for the mean and median, f)  $28 \text{ \AA}^{-1}$ to  $31 \text{ \AA}^{-1}Q$  range for the standard deviation . . . . . 38

Figure 4.18 Masking, average, and standard deviation of an example x-ray total scattering measurement. This image was produced with only an edge mask. a) the image, b) the mask, c) the mean and median values, d) the standard deviation (normalized to the median), e) a closeup of the  $28 \text{ \AA}^{-1}$ to  $31 \text{ \AA}^{-1}Q$  range for the mean and median, f)  $28 \text{ \AA}^{-1}$ to  $31 \text{ \AA}^{-1}Q$  range for the standard deviation . . . . . 39

Figure 4.19 Masking, average, and standard deviation of an example x-ray total scattering measurement. This image was produced combining an edge mask and the automatically generated mask. a) the image, b) the mask, c) the mean and median values, d) the standard deviation (normalized to the median), e) a closeup of the  $28 \text{ \AA}^{-1}$ to  $31 \text{ \AA}^{-1}Q$  range for the mean and median, f)  $28 \text{ \AA}^{-1}$ to  $31 \text{ \AA}^{-1}Q$  range for the standard deviation . . . . . 40

## TODO LIST

2	Why is atomistic engineering important . . . . .	2
3	Barriers to atomistic engineering . . . . .	2
4	How are we going to attack this problem . . . . .	2
5	Fix the figures so that they don't give the full caption . . . . .	4

6

## INTRODUCTION

7

### Why is atomistic engineering important

8     Engineering materials and chemicals on the atomic scale has been a goal for the  
9     chemistry, physics, materials science, and chemical engineering fields long before the  
10    advent of nanomaterials. Realizing this goal could lead to durable fuel cell catalysts,  
11    more bioavailable pharmaceuticals, and radiation damage resistant spacecraft shielding.

12

### Barriers to atomistic engineering

13    Before we can even think of making atomistically exact structures, durable struc-  
14    tures, or structures which change in reproducible ways, we need to know the atomic  
15    structure exactly.

16    How are we going to attack this problem

17    This work addresses these issues by developing a methodology for solving the  
18    structure of nanomaterials by matching experimental x-ray scattering data with sim-  
19    ulated atomic structures.

20    Chapter 1 develops the statistical mechanical system used to match the theoretical  
21    structure. §1.2 focuses on the development of potential energy surfaces, including  
22    potential energy and force equations, which have minima where experimental results  
23    and simulated structures agree the most. §1.3 will discuss statistical mechanical  
24    ensembles which are used to search for minima on the potential energy surface.

25    Chapter 2 will discuss the mathematical and computational development of the  
26    atomic pair distribution function (PDF). §2.2 will focus on the rapid graphical pro-  
27    cessing unit based calculation of the PDF and its gradients.

28    Chapter 3 will discuss the benchmarking of the the combined statistical mechan-

29 ical optimizer and PDF calculation systems against a series of theoretical nanoparti-  
30 cles, focusing on understanding limitations of the method and structure reproduction.

31 Chapter 4 will focus on the aquesition of experimental data, its management, and  
32 processing. §4.2, 4.2, and 4.2 will discuss the derivation of the  $Q$  resolution function,  
33 the automated masking of 2D area detectors for x-ray total scattering measurements  
34 using the previously derrived  $Q$  resolution, and the impact of different averaging  
35 methods and masks on azimuthal integration, respecitvly.

Fix the  
figures  
so that  
they  
don't  
give  
the full  
caption

37

# CHAPTER 1

38

## STATISTICAL MECHANICAL ENSEMBLES AND POTENTIAL ENERGY SURFACES

40 1.1 INTRODUCTION

41 The approach taken in this work for solving the atomic structures of materials is  
42 one of optimization. The positional variables of the system are optimized so as to  
43 minimize the value of a potential energy surface (PES). The

44 1.2 POTENTIAL ENERGY SURFACES

45 A PES simply describes the potential energy of the system as a function of all its  
46 relevant coordinates in phase space, essentially providing a mapping  $\mathbb{R}^n \rightarrow \mathbb{R}$ . Usually  
47 these coordinates are the positions of the atoms  $q$  and their conjugate momenta  $p$ .  
48 Note that there could be more variables associated with the system, for instance the  
49 magnetic moments of the atoms could play a role in describing the system. In this  
50 magnetic system there would be positional variables for the atomwise spin vectors  
51 and their "momenta". Application of the term "momenta" might seem odd here, as  
52 the magnetic spin does not have a mass or a velocity. However, since the magnetic  
53 "position" is defined on the PES we need to describe its conjugate variable to properly  
54 formulate Hamiltonian dynamics and the kinetic portion of the PES.

55 **Experimentally Derived Potential Energy Surfaces**

56 Generally PESs are obtained from purely computational experiments including: ab-  
 57 initio DFT, classical approximations via the embedded atom method, or even param-  
 58 eter driven models with experimentally fitted parameters. However, one can derive  
 59 a PES from an experiment which describes how well the model reproduces the ex-  
 60 perimental data. In this case one needs a theoretical and computational framework  
 61 mapping the atomistic variables of the simulation to the same space of the data ob-  
 62 tained from the experiment. This allows the experiment to be compared directly  
 63 against the predicted data via an experimentally derived PES.

64 **Potentials**

65 For an experiment which produces 1D data, like powder diffraction, EXAFS or XPS,  
 66 the implemented potentials are:

$$\chi^2 = \sum_{a=a_{\min}}^{a_{\max}} (A_{\text{obs}} - \alpha A_{\text{calc}})^2 \quad (1.1)$$

$$Rw = \sqrt{\frac{\sum_{a=a_{\min}}^{a_{\max}} (A_{\text{obs}} - \alpha A_{\text{calc}})^2}{\sum_{a=a_{\min}}^{a_{\max}} A_{\text{obs}}^2}} \quad (1.2)$$

$$\chi_{\text{INVERT}}^2 = \frac{1}{N} \sum_j \sum_r [A_{\text{obs}}(r) - \alpha A_{j,\text{calc}}(r)]^2 \quad (1.3)$$

$$\alpha = \frac{\sum_{a=a_{\min}}^{a_{\max}} A_{\text{obs}} A_{\text{calc}}}{\sum_{a=a_{\min}}^{a_{\max}} A_{\text{calc}}^2} = \frac{\vec{A}_{\text{obs}} \cdot \vec{A}_{\text{calc}}}{|\vec{A}_{\text{calc}}|^2} \quad (1.4)$$

70 where  $A_{\text{calc}}$  and  $A_{\text{obs}}$  are the calculated and observed 1D experimental data and  $A_{\text{calc},j}$   
 71 is the calculated data for a single atom interacting with the other atoms of the system.  
 72 Note that  $A_{\text{calc}}$  has a dependence on  $q$ , the positions of the system.

73 **Forces**

$$\vec{\nabla} \chi^2 = -2 \sum_{a=a_{\min}}^{a_{\max}} (\alpha \frac{\partial A_{\text{calc}}}{\partial \gamma_{i,w}} + A_{\text{calc}} \frac{\partial \alpha}{\partial \gamma_{i,w}})(A_{\text{obs}} - \alpha A_{\text{calc}}) \quad (1.5)$$

74

$$\vec{\nabla}Rw = \frac{Rw}{\chi^2} \sum_{a=a_{\min}}^{a_{\max}} (\alpha \frac{\partial A_{\text{calc}}}{\partial \gamma_{i,w}} + A_{\text{calc}} \frac{\partial \alpha}{\partial \gamma_{i,w}})(\alpha A_{\text{calc}} - (A_{\text{obs}})) \quad (1.6)$$

75

$$\frac{\partial \alpha}{\partial \gamma_{i,w}} = \frac{(\sum_{a=a_{\min}}^{a_{\max}} A_{\text{obs}} \frac{\partial A_{\text{calc}}}{\partial \gamma_{i,w}} - 2\alpha \sum_{a=a_{\min}}^{a_{\max}} A_{\text{calc}} \frac{\partial A_{\text{calc}}}{\partial \gamma_{i,w}})}{\sum_{a=a_{\min}}^{a_{\max}} A_{\text{calc}}^2} \quad (1.7)$$

76

$$\vec{\nabla}\chi^2_{\text{INVERT}} = \frac{-2}{N} \sum_{a=a_{\min}}^{a_{\max}} \sum_j (\alpha \frac{\partial A_{j,\text{calc}}}{\partial \gamma_{i,w}} + A_{j,\text{calc}} \frac{\partial \alpha}{\partial \gamma_{i,w}})(A_{\text{obs}} - \alpha A_{j,\text{calc}}) \quad (1.8)$$

77 where  $\gamma_{i,w}$  is the  $i$ th arbitrary positional variable in the  $w$ th direction. The concept  
 78 of an "arbitrary positional variable" might seem a bit cumbersome but it allows us  
 79 to define the forces for any atomic parameter which can be represented as a vector  
 80 in 3-space. This comes in handy when trying to define the forces acting on variables  
 81 like anisotropic displacement parameters or atomic magnetic spins.

82 DISCUSS INVERT A BUNCH. ALSO COMPARE RW AND CHI\*\*2, POTEN-  
 83 TIALY WITH A FIGURE.

84 1.3 ENSEMBLES

85 While PESs describe which atomic configurations are the most desirable and how  
 86 the atoms would like to get there, the ensemble describes how the atoms move on  
 87 the PES. The abstraction of the PES from the ensemble is an important one, as it  
 88 allows for the reuse and exchange of both PESs and ensembles for a wide array of  
 89 problems. Statistical mechanical ensembles can be described in two ways, analytically  
 90 and stochastically. For long simulation times and fine enough numerical or analytical  
 91 integration these two descriptions should be identical. In either case one starts by  
 92 defining the Hamiltonian  $\mathcal{H}$  as the total energy of the system. Thus, the Hamiltonian  
 93 is described as the sum of the potential  $U(q)$  and kinetic  $K(p)$  energies, where  $q$  is  
 94 the positions of the atoms and  $p$  is their momenta

$$\mathcal{H}(q, p) = U(q) + K(p) \quad (1.9)$$

95 where  $K(p) = \frac{1}{2} \sum_i \frac{p_i^2}{m_i}$  and  $i$  denotes the  $i$ th particle. Analytically one generally defines  
 96 a partition function, which describes the sum of probabilities over all potential atomic  
 97 states.

$$\Xi = \sum_i P_i(q, p)$$

98 where  $P_i$  is the probability of the  $i$ th state and is a function of the total energy of  
 99 that state. This partition function can then be used to obtain the probability of any  
 100 specific state.

## 101 Hamiltonian Monte Carlo

In order to model dynamics we need to describe the motion of the particles in our system, thus:

$$\frac{dq_i}{dt} = \frac{\partial \mathcal{H}}{\partial p_i} = p_i \quad (1.10)$$

$$\frac{dp_i}{dt} = -\frac{\partial \mathcal{H}}{\partial q_i} = -\vec{\nabla}U \quad (1.11)$$

Using these equations we can derive the position and momentum vectors at any point in time using the leap-frog algorithm:

$$p_i(t + \delta t/2) = p_i(t) - \frac{\delta t}{2} \frac{\partial}{\partial q_i} U(q(t)) \quad (1.12)$$

$$q_i(t + \delta t) = q_i(t) + \delta t * p_i(t + \delta t/2) \quad (1.13)$$

$$p_i(t + \delta t) = p_i(t + \delta t/2) - \frac{\delta t}{2} \frac{\partial}{\partial q_i} U(q(t + \delta t)) \quad (1.14)$$

102 Note that  $\frac{\partial}{\partial q_i}$  is the gradient with respect to  $q$  where  $i$  denotes the  $i$ th atom being  
 103 moved. Using this notation the gradient is

$$\vec{\nabla}U = \begin{bmatrix} \frac{\partial U}{\partial q_{0,x}} & \frac{\partial U}{\partial q_{0,y}} & \frac{\partial U}{\partial q_{0,z}} \\ \vdots & \frac{\partial U}{\partial q_{i,w}} & \vdots \\ \frac{\partial U}{\partial q_{n,x}} & \frac{\partial U}{\partial q_{n,y}} & \frac{\partial U}{\partial q_{n,z}} \end{bmatrix} = \begin{bmatrix} \vec{\mathcal{F}}_0 \\ \vdots \\ \vec{\mathcal{F}}_i \\ \vdots \\ \vec{\mathcal{F}}_n \end{bmatrix} \quad (1.15)$$

104 where  $\frac{\partial}{\partial q_{i,w}}$  is the derivative with respect to  $q$  where  $w$  denotes direction of the deriva-  
 105 tive ( $x$ ,  $y$ , or  $z$ ),  $n$  is the number of atoms and  $U$  is the potential which depends on  
 106  $q$ , and  $\vec{F}_i$  is the "force" on the  $i$ th atom.

107 **No-U-Turn-Sampling**

108 **Grand Canonical Ensemble**

109 **Ensemble description**

110 In the Grand Canonical Ensemble (GCE) two sets of variables are allowed to change,  
 111 the atomic positions and the total number of atoms and their associated identities.  
 112 These two variables are controlled by temperature and chemical potential. The par-  
 113 tition function is

$$\Xi = e^{-\beta(\mathcal{H}+\mu)} \quad (1.16)$$

114 This is translated into a Monte Carlo system, producing Grand Canonical Monte  
 115 Carlo (GCMC).

116 **Grand Canonical Monte Carlo**

117 While the probabilities for atomic motion are the same as in the Canonical Ensemble,  
 118 the addition or removal of an atom have their own probabilities. For the addition of  
 119 an atom the probability is formally:

$$\min[1, \frac{V}{(N+1)\Lambda(T)^3} e^{-\beta\Delta U + \beta\mu}] \quad (1.17)$$

120 Similarly the removal of an atom has the probability:

$$\min[1, \frac{(N)\Lambda(T)^3}{V} e^{-\beta\Delta U - \beta\mu}] \quad (1.18)$$

121 However, both of these equations depend of the overall simulation volume and the  
 122 thermal wavelength, which is undesirable as these are not really properties that we

123 are of interest to these simulations. Thus, we roll them into the definition of the  
124 chemical potential, essentially setting the base chemical potential to counteract these  
125 effects. This makes certain that our simulation does not change if we change the  
126 overall cell volume. A GCMC move consists of creating a new atomic configuration,  
127 where an atom has been added or removed, and checking the above criteria. However,  
128 previous results have shown that this method is computationally expensive in dense  
129 liquids, and exceedingly expensive in solid materials. The long simulation times  
130 are due to the random nature of the atomic additions or removals which produce:  
131 over-tightly packed atoms, atoms in the middle of nowhere, or unphysical vacancies.  
132 These configurations are rejected by the GCMC criteria but their probability of being  
133 sampled is much higher than configurations which are lower in energy, since the  
134 number of incorrect ways to add/remove atoms is much larger than the correct ways.  
135 Thus we have implemented methods for biasing the atomic addition positions and  
136 the atomic removals toward configurations which are more likely to be accepted.

### 137 GCMC biasing

138 The first method is to remove some of the excess options from the probability pool.  
139 Initially the insertion positions are calculated at random using a random number gen-  
140 erator and scaled to the size of the simulation cell. This produces probabilities which  
141 have floating point level precision, which is effectively infinite. While this produces  
142 a potentially infinite number of ways to create energetically favorable configurations,  
143 the infinite ways to produce bad configurations is much larger. Thus we can limit this  
144 by moving to voxels. In this case atoms are added to the center of voxels which have  
145 a pre-set resolution, limiting our total number of valid addition points. While this  
146 could produce some problems with ergodicity, we avoid this by allowing the atoms to  
147 translate throughout the system. Each voxel has a probability of being tried:

$$P_{i,j,k} = \frac{xyz}{abc} \quad (1.19)$$

148 where  $x, y, z$  and  $a, b, c$  are the resolutions and cell side lengths in the cardinal di-  
149 rections, respectively. While this does help to limit the total probability space it  
150 does not tell us which voxels are likely to lead to better configurations, leading to  
151 many rejected atomic additions. To combat this issue we can weigh the individual  
152 voxels, giving more probability to voxels which show promise and less to those with  
153 less likelihood to be accepted.

154 The approach most likely to yield success would be to measure the change in  
155 potential energy associated with the addition of an atom at the center of the voxel  
156 where the probability of a voxel to be tried is:

$$P_{i,j,k} = \frac{e^{\beta\Delta U_{i,j,k}}}{\sum_{i,j,k} e^{\beta\Delta U_{i,j,k}}} \quad (1.20)$$

157 where  $\Delta U_{i,j,k}$  is the change in energy. However, calculating  $\Delta U_{i,j,k}$  can be particu-  
158 larly expensive, especially when calculating scattering from atomic positions. The  
159 computational expense can be mitigated by using a cheaper potential, if only for the  
160 evaluation of the voxel energy, as previously shown. Similar to previous work we can  
161 use the Lennard Jones potential to approximate the addition potential.

162

## CHAPTER 2

163

### ATOMIC PAIR DISTRIBUTION FUNCTION:

164

### THEORY AND COMPUTATION

165 2.1 THEORY

166 To properly understand the PDF and its limitations we need to derive its mathemat-  
167 ics. The following derivation has been performed numerous times but most recently  
168 and completely by Farrow and Billinge, it is reproduced here for clarity and com-  
169 pleteness.

170 **Derivation**

171 **Analytical Gradients**

172 Many optimization algorithms and simulations methodologies, including HMC, re-  
173 quire not only the potential energy of a given configuration but also the forces acting  
174 on that configuration. These forces are described by the gradient of potential energy  
175 of the system which in turn requires the gradient of the PDF. As previously shown the  
176 PDF is the Fourier Transform of the Debye equation. Since the Fourier Transform is  
177 expressed as an integral we can exchange the order of the gradient and the integral,  
178 allowing us to calculate the analytical gradient of the Debye equation and FFT the  
179 resulting function. The Debye equation, with a Debye-Waller vibrational correction  
180 is

$$F(Q) = \frac{1}{N\langle f \rangle^2} \sum_{j \neq i} f_i^*(Q) f_j(Q) \exp(-\frac{1}{2}\sigma_{ij}^2 Q^2) \frac{\sin(Qr_{ij})}{r_{ij}} \quad (2.1)$$

181 where

$$\sigma_{ij}^2 = (\vec{u}_{ij} * \hat{d}_{ij})^2 \quad (2.2)$$

$$\vec{u}_{ij} = \vec{u}_i - \vec{u}_j \quad (2.3)$$

$$\hat{d}_{ij} = \frac{\vec{d}_{ij}}{r_{ij}} \quad (2.4)$$

$$r_{ij} = \|\vec{d}_{ij}\| \quad (2.5)$$

$$\vec{d}_{ij} = \begin{bmatrix} q_{ix} - q_{jx} \\ q_{iy} - q_{jy} \\ q_{iz} - q_{jz} \end{bmatrix} \quad (2.6)$$

182 where  $Q$  is the scatter vector,  $f_i$  is atomic scattering factor of the  $i$ th atom, and  $r_{ij}$   
 183 is the distance between atoms  $i$  and  $j$  and has  $q$  dependence. For simplicities sake  
 184 we will break up  $F(Q)$  so that

$$F(Q) = \alpha \sum_{j \neq i} \beta_{ij} \tau_{ij} \Omega_{ij} \quad (2.7)$$

185 where

$$\alpha = \frac{1}{N\langle f \rangle^2} \quad (2.8)$$

$$\beta_{ij} = f_i^*(Q) f_j(Q) \quad (2.9)$$

$$\tau_{ij} = \exp(-\frac{1}{2} \sigma_{ij}^2 Q^2) \quad (2.10)$$

$$\Omega_{ij} = \frac{\sin(Qr_{ij})}{r_{ij}} \quad (2.11)$$

186 The derivatives are as follows:

$$\frac{\partial}{\partial q_{i,w}} F(Q) = \alpha \sum_j \beta_{ij} \left( \frac{\partial \tau_{ij}}{\partial q_{i,w}} \Omega_{ij} + \tau_{ij} \frac{\partial \Omega_{ij}}{\partial q_{i,w}} \right) \quad (2.12)$$

187 where

$$\frac{\partial \Omega_{ij}}{\partial q_{i,w}} = \frac{Q \cos(Qr_{ij}) - \Omega_{ij}}{r_{ij}^2} (q_{i,w} - q_{j,w}) \quad (2.13)$$

$$\frac{\partial \tau_{ij}}{\partial q_{i,w}} = \frac{\sigma_{ij} Q^2 \tau_{ij}}{r_{ij}^3} ((q_{i,w} - q_{j,w}) \sigma_{ij} - (u_{i,w} - u_{j,w}) r_{ij}^2) \quad (2.14)$$

188 Since  $\vec{u}_{ij}$  is a variable as well, we need the derivative with respect to it as well.

189 Thus

$$\frac{\partial}{\partial u_{i,w}} F(Q) = \alpha \sum_j \beta_{ij} \frac{\partial \tau_{ij}}{\partial u_{i,w}} \Omega_{ij} \quad (2.15)$$

$$\frac{\partial \tau_{ij}}{\partial u_{i,w}} = -\frac{\sigma_{ij} Q^2 \tau_{ij}}{r_{ij}} (q_{i,w} - q_{j,w}) \quad (2.16)$$

190 **Without ADPs**

191 Without ADPs the equations simplify down to

$$F(Q) = \frac{1}{N \langle f \rangle^2} \sum_{j \neq i} f_i^*(Q) f_j(Q) \frac{\sin(Qr_{ij})}{r_{ij}} \quad (2.17)$$

192 and

$$\frac{\partial}{\partial q_{i,w}} F(Q) = \alpha \sum_j \beta_{ij} \frac{\partial \Omega_{ij}}{\partial q_{i,w}} \quad (2.18)$$

193 use of these equations, when ADPs are not appropriate (like at cryogenic tempera-  
194 tures), greatly speeds up the computaiton.

195 **2.2 COMPUTATION**

196 Simply deriving the equations for the PDF is not enough. The many body nature of  
197 the PDF equation make analytical solution of the structure from the PDF impossible.  
198 Thus, the PDF must be computed from a structural candidates and compared against  
199 experimental results to evaluate the reliability of the model.

200 **HPC and GPUs**

201 To properly solve the structure of materials the PDF will need to be computed many  
202 times and checked against experimental results. This requires computation of the  
203 PDF, potentialy over many atoms. Calculating these PDFs requires a fast, highly  
204 parallized, computational framework.

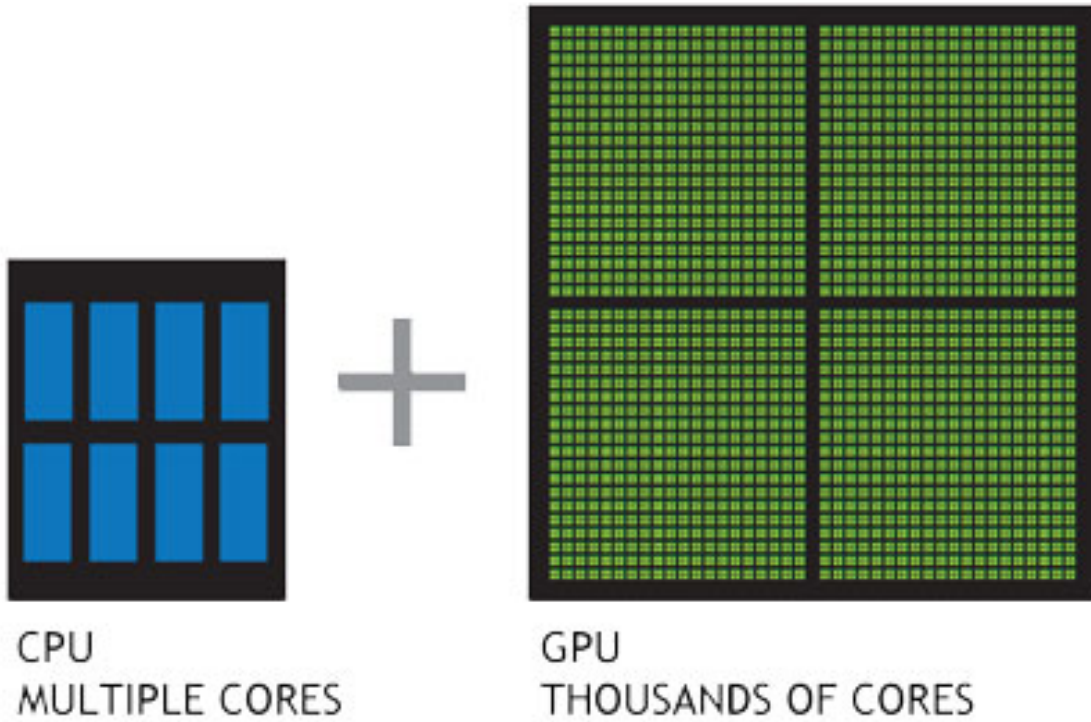


Figure 2.1: Comparison of the CPU and GPU chip architectures

## 205 GPUs and Parallelization

206 Computing the PDF is an embarrassingly parallel problem. The basic procedure is  
 207 to calculate the reduced structure factor  $F(Q)$  for each atom pair and momentum  
 208 transfer vector, sum over all the atom pairs, and Fourier transform the structure to  
 209 the PDF. The first part of this procedure is perfectly parallelizable, as each atom pair is  
 210 separate from the others. The summation over all the atomic reduced structure factors  
 211 can be parallelized via distributed summing. Lastly the FFT can be parallelized using  
 212 existing parallel FFT algorithms.

213 GPUs are particularly well suited to the task of computing PDFs. GPU chip  
 214 architecture is designed to perform many tasks simultaneously by having potentially  
 215 thousands of cores.

216 Map from  $ij$  space to  $k$  space

217 The above equations, although formally correct, are very ineffiecent.  $F(Q)$  and its  
 218 gradient are indexed over all the atoms twice, however there are symmetries that  
 219 allow us to only compute over the atom pairs esentially mapping from an  $n \times n$  space,  
 $ij$  space, to a  $\frac{n(n-1)}{2}$  space,  $k$  space. For  $F(Q)$  we apply the following mapping where

$$\begin{array}{ccccc} & & \psi & & \\ E & \xrightarrow{\quad} & E' & \xrightarrow{\Sigma} & Z \\ \phi \downarrow & & & \nearrow \Sigma' & \\ B & \xrightarrow{\quad} & B' & & \end{array}$$

220

221  $E$  denotes the atomic coordinates in  $ij$  space,  $E'$  denotes  $F(Q)$  before the summation  
 222 in  $ij$  space,  $B$  denotes the atomic pairs in  $k$  space,  $B'$  denotes  $F(Q)$  in  $k$  space, and  
 223  $Z$  denotes the final summed  $F(Q)$ . For the operators,  $\phi$  denotes the mapping from  
 224  $ij$  space to  $k$  space  $k = j + i * \frac{i-1}{2}$ ,  $\psi$  and  $\psi'$  denote the  $F(Q)$  operation in  $ij$  and  $k$   
 225 space, respectivly.  $\Sigma$  denotes the sum over all the atoms.

226 To properly define  $\Sigma'$  we must establish whether  $F(Q)$  is an even function. We  
 227 can accomplish this by examining each of the portions of  $F(Q)$ ,  $\alpha, \beta, \tau, \Omega$ .  $\Omega$  is even,  
 228 since  $r_{ij}$  is the interatomic distance, which is the same despite a flip of indicies,  $Q$   
 229 does not depend on the atomic indicies, and since  $Qr_{ij}$  is even so is  $\sin Qr_{ij}$ . Thus,  
 230  $\Omega$  is even. Providing similar analysis to  $\tau$  we can see that while  $\vec{u}_{ij}$  is odd, so is  
 231 the unit displacement vector between the two atoms, thus the two odds cancel out.  
 232 Intuitivly this makes sense, since the  $F(Q)$  equation is fundamentally interested in the  
 233 interatomic distances which is even. Thus, switching atom indicies does not change  
 234  $F(Q)$ . Due to the even nature of the  $F(Q)$  operator the  $\Sigma'$  operator sums over all the  
 235 atom pairs, and multiplies by two to reflect the double counting of the  $\Sigma$  operator.

236 For the gradient a similar mapping is used:

237 In this mapping, however, we use the  $\tilde{\phi}\Sigma$  operator. This operator simultaniously

$$\begin{array}{ccccc}
& & \psi & & \Sigma \\
E & \xrightarrow{\quad} & E' & \xrightarrow{\quad} & Z \\
\phi \downarrow & & & \nearrow \tilde{\phi}\Sigma & \\
B & \xrightarrow{\quad} & B' & & 
\end{array}$$

238 performs a reverse mapping from  $k$  to  $ij$  space, and a summation with the correct  
 239 symmetry. In this case the  $\psi$  and  $\psi'$  operators, which denote the  $\vec{\nabla}F(Q)$  operator  
 240 in  $ij$  and  $k$  space, are antisymmetric. Intuitivly this makes sense as an extension of  
 241 Newton's Second Law, since each particle's interation is felt oppositely by its partner.

## 242 Periodic Boundary Conditions

243 Periodic boundary conditions can be helpful when simulating extended solids or large  
 244 nanoparticles. In this case all the non-crystallinity is contained within the simulation  
 245 box and the box is repeated to create the longer distance peaks observed in the PDF.  
 246 To perform this we can break up the Debye equation into two main parts, the part  
 247 that describes the interatomic distances within the simulation box and those between  
 248 boxes. Neglecting the thermal motion portion:

$$F(Q) = \frac{1}{N\langle f \rangle^2} \left( \sum_{j \neq i} f_i^*(Q) f_j(Q) \frac{\sin(Qr_{ij})}{r_{ij}} + \sum_{i,j} f_i^*(Q) f_j(Q) \frac{\sin(QR_{ij})}{R_{ij}} \right) \quad (2.19)$$

249 where

$$R = |\vec{r} + \vec{u}| \quad (2.20)$$

$$\vec{u} = \gamma_1 * \vec{a} + \gamma_2 * \vec{b} + \gamma_3 * \vec{c} \quad (2.21)$$

250

## CHAPTER 3

251

### BENCHMARKING

252 3.1 PDF

253 **Au55: surface relaxed**

254 **Au55: surface disordered**

255 **Au55: amorphous**

256 **Au102: triple phase**

257 **FCC**

258 **Marks decahedron**

259 **Au147**

260 3.2 PDF WITH ADPs

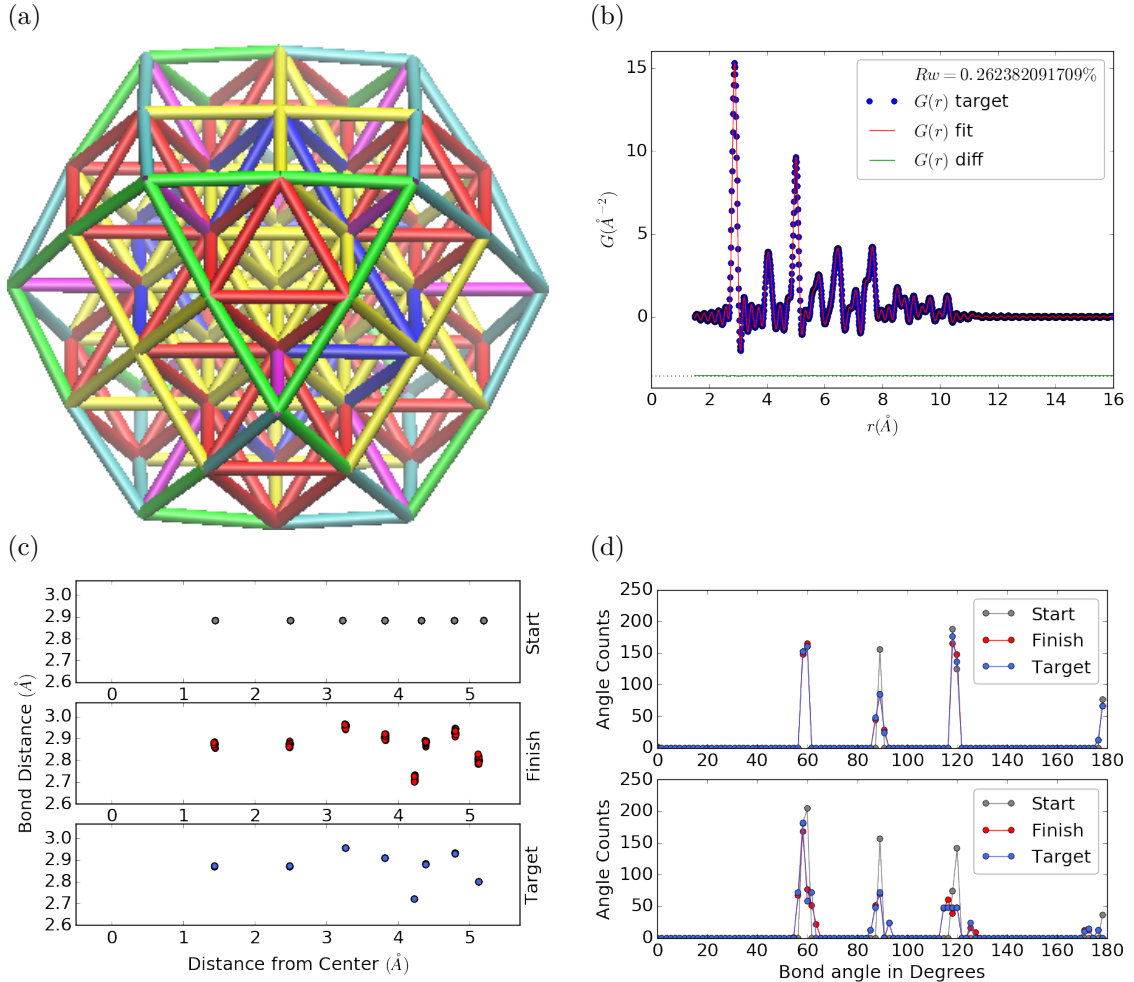


Figure 3.1: Au<sub>55</sub> PDF fitting of DFT-optimized  $c$ -Au<sub>55</sub>. a) the final structural solution ( $Rw=0.3\%$ ) with bond lengths color-coded by step of 0.05\text{\AA}, b) the target PDF(blue dots) overlaid with the PDF of the final structure (solid red lines) with the difference in green lines offset below, c) the radial bond distribution, and d) bond angle distribution.

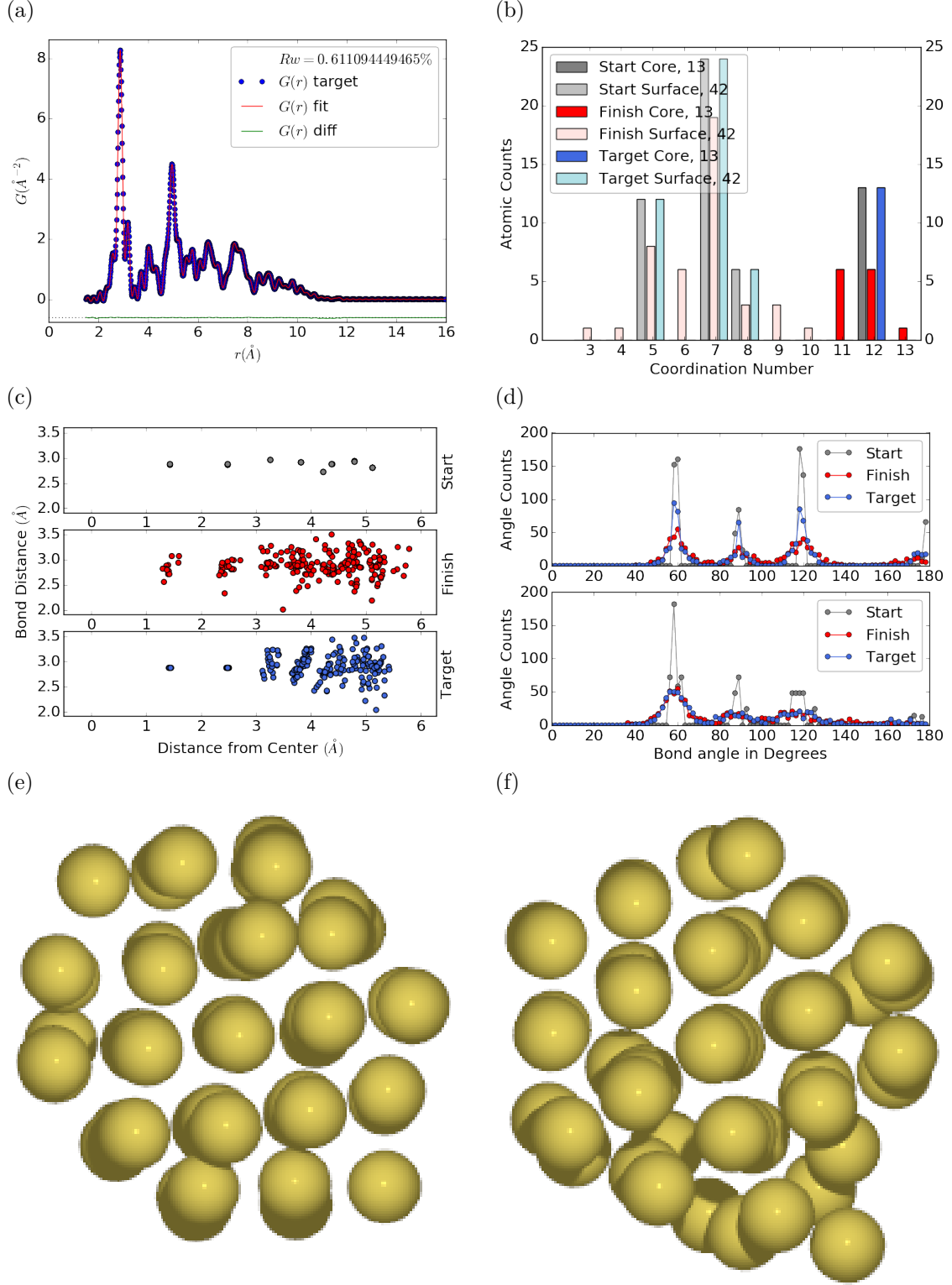


Figure 3.2:  $\text{Au}_{55}$  PDF fitting of surface-disordered  $\text{Au}_{55}$ . a) the target structure, b) the final structural solution ( $Rw=0.6\%$ ), c) the comparison of PDFs, d) the CN distribution with the number of atoms in either the core or the surface, e) the radial bond distribution, and f) the bond angle distribution.

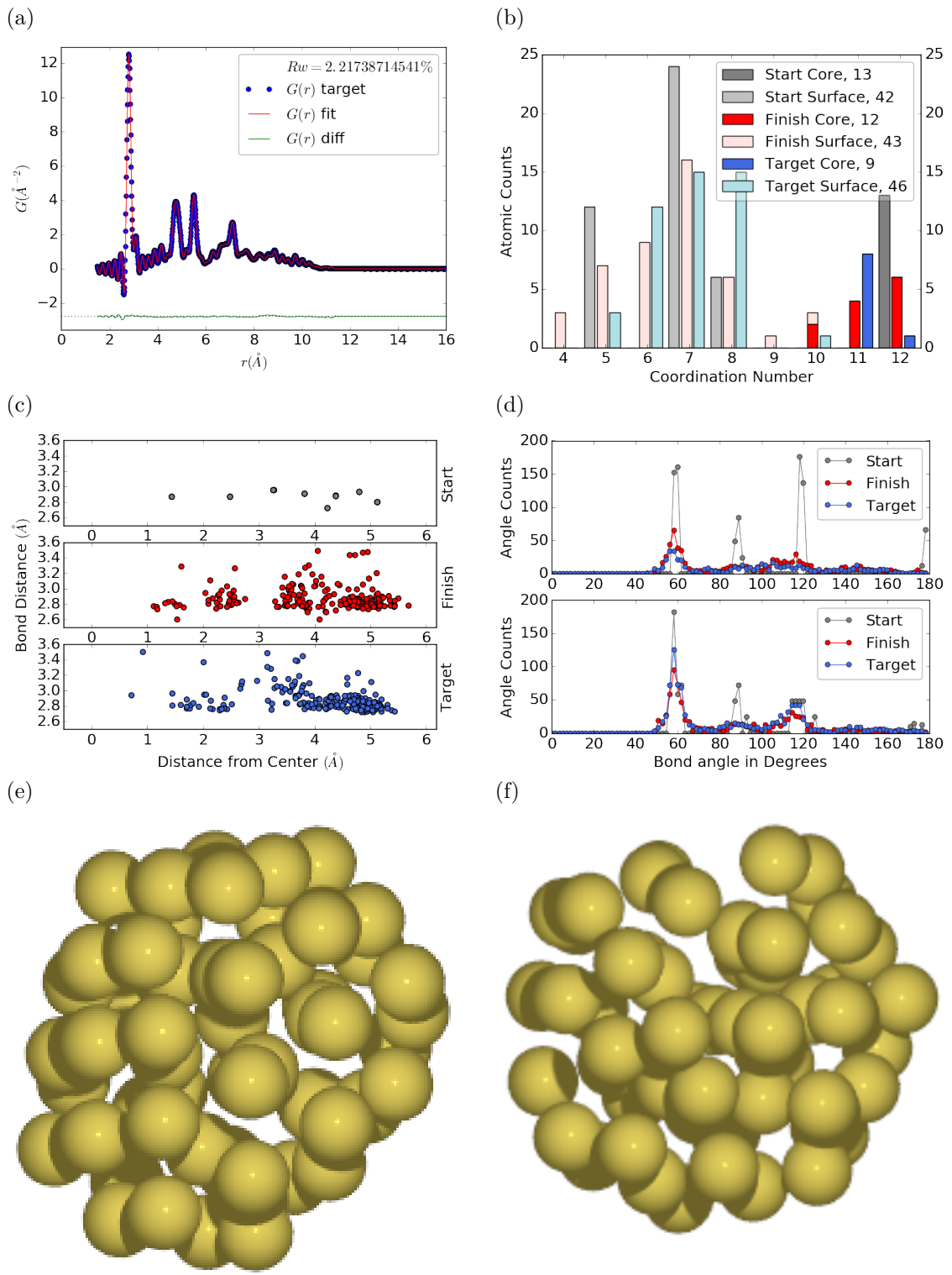


Figure 3.3: Similar to figure 3.2 for DFT-optimized amorphous  $\text{Au}_{55}$ .

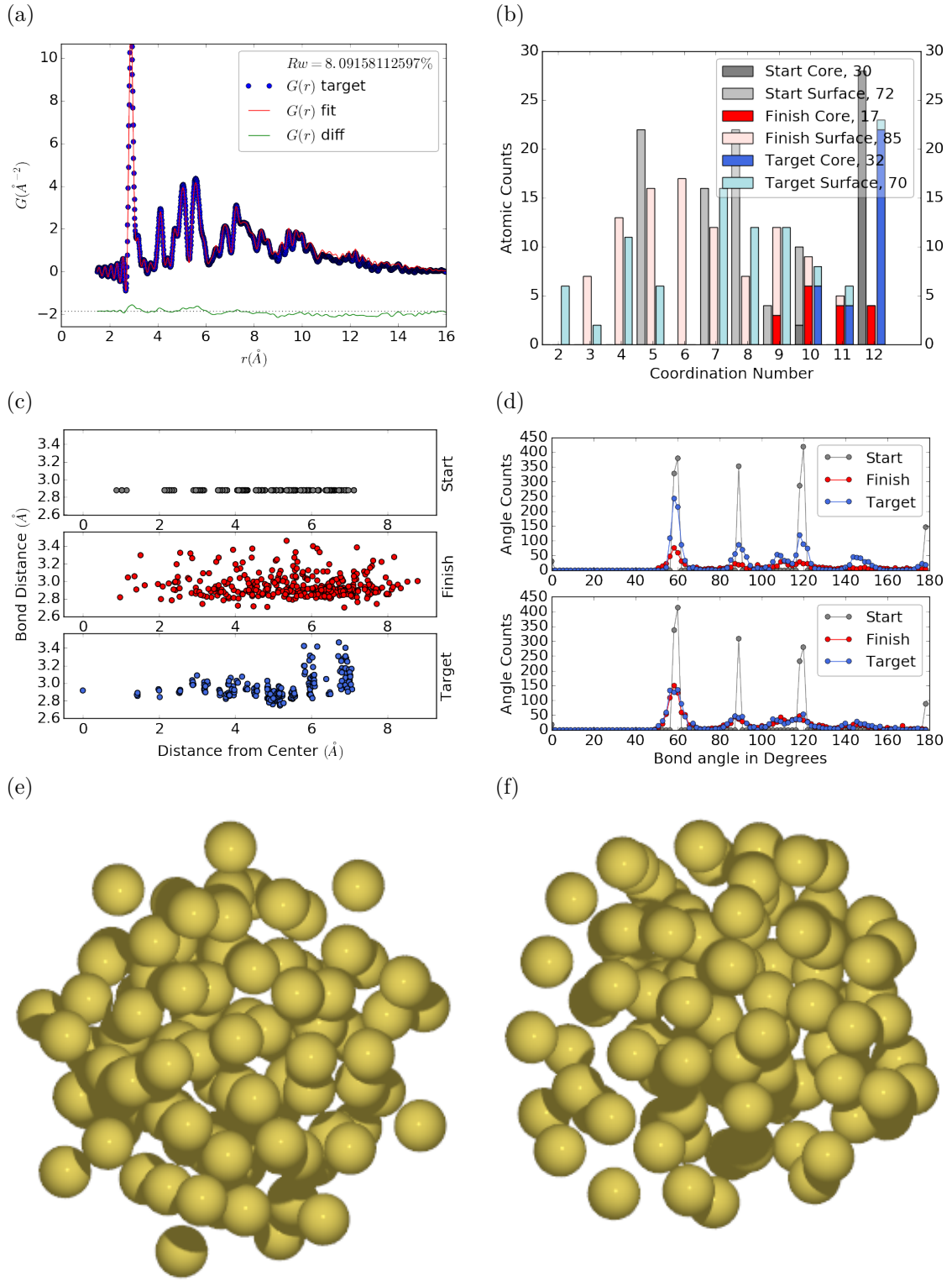


Figure 3.4: Similar to figure 3.2 for  $\text{Au}_{102}$  as in DFT-optimized  $\text{Au}_{102}\text{MBA}_{44}$  cluster.

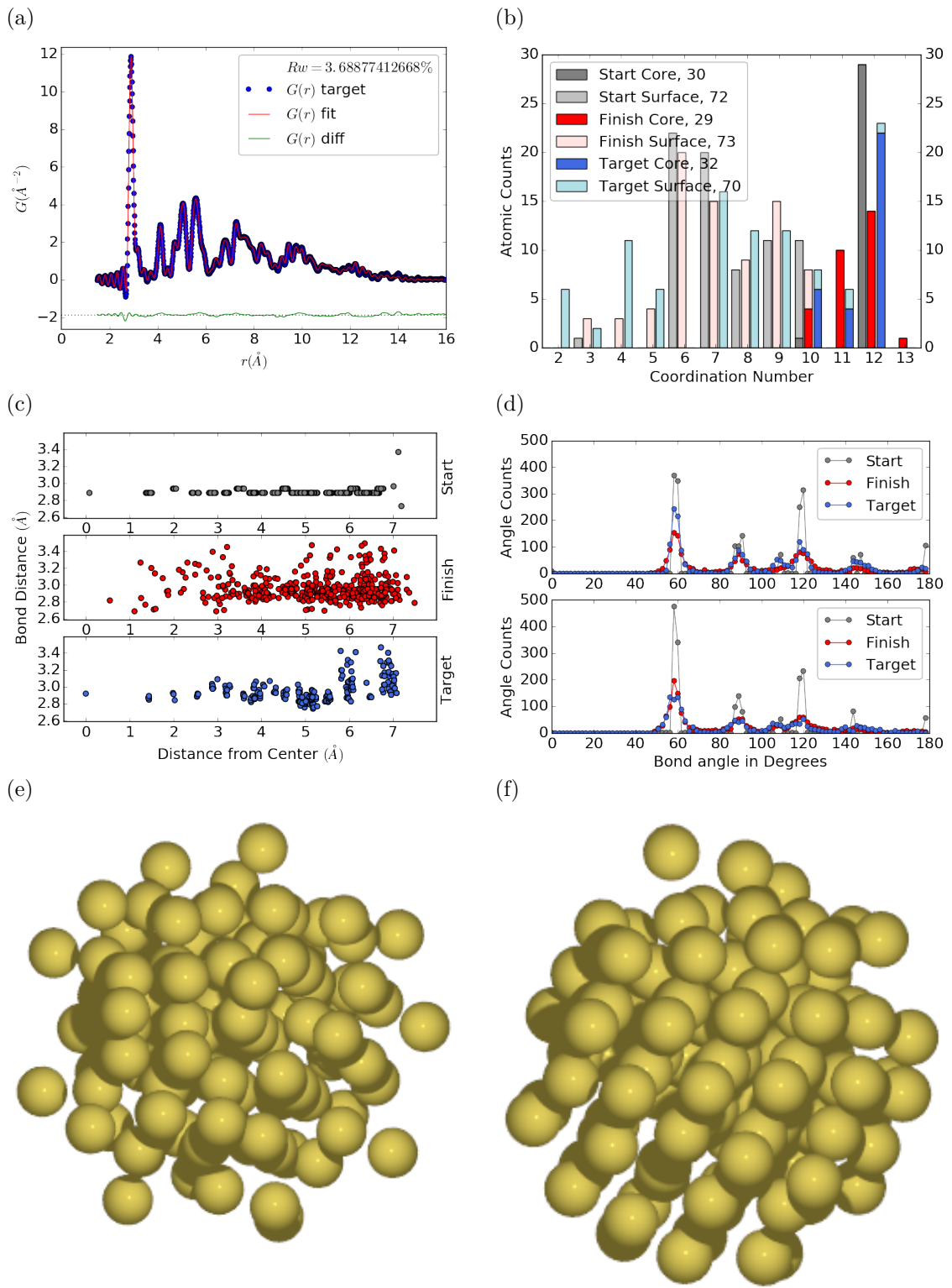


Figure 3.5: Similar to Fig. 3.4 with Marks decahedron as the starting structure.

261

## CHAPTER 4

262

# X-RAY TOTAL SCATTERING DATA ACQUISITION AND 263 PROCESSING

264 4.1 EXPERIMENT

265 PDF experiments are generally performed at synchrotron light sources, as only these  
266 sources can provide the needed flux, energy, and high momentum transfer vectors needed  
267 to obtain reliable PDFs.

268 4.2 DATA PROCESSING WORKFLOW

269 Processing the raw pixel intensities to the PDF is very important as we are extracting  
270 most of our interesting information out of very high  $Q$  data. This data relies on good  
271 statistics and sound background subtraction. Talk about papers from Billinge Group  
272 with thin film PDF and dilute NP solutions. Diagram of the overall data processing  
273 workflow. Discuss the NSLS-II data stack.

274 **MetadataStore Side Loading**

275 Design of sidewinder-spec for loading the data into metadatastore. Most of the design  
276 considerations went into the loaders, which are different for each experiment.

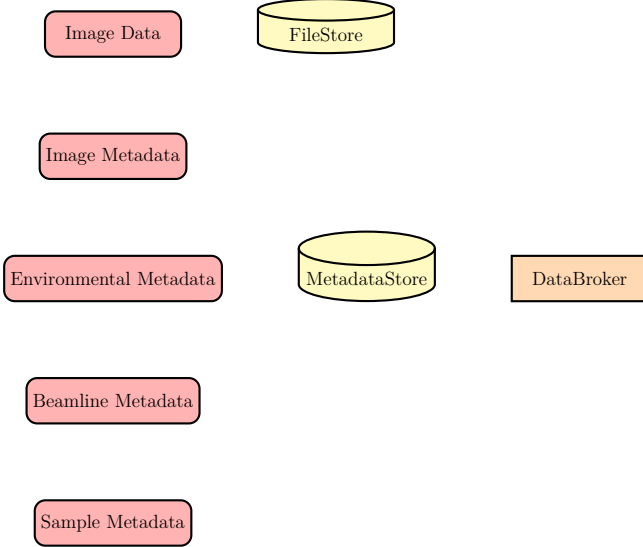


Figure 4.1: Database Loading Workflow. Data is loaded from various sources, including images and text files, into the FileStore and MetadataStore databases. Data is then retrieved from the databases using the databroker.

## 277 Detector $Q$ resolution

278 To properly azimuthally integrate the images taken from the detector the  $Q$  resolution  
 279 of the pixels must be calculated. Integrating using even bins will cause pixels which  
 280 are not on the same ring to be binned together, causing the incorrect value of  $I(Q)$   
 281 to be obtained and a larger standard deviation in the integrated data. To properly  
 282 calculate the  $Q$  resolution the resolution of each of the pixels in  $2\theta$  must be calculated.  
 283 Figure 4.2 shows the scattering of x-rays onto a flat image plate detector. In this  
 284 diagram the bottom of the  $n$ th pixel is  $B$  while the top is  $B'$ . The resolution of this  
 285 pixel in  $2\theta$  is  $\angle BAC - \angle B'AC$ . Thus the resolution, calculated from the distances is

$$\Delta 2\theta = \arctan \frac{b}{d} - \arctan \frac{t}{d} \quad (4.1)$$

286 where  $d$  is the sample to detector distance,  $b$  is the distance to the bottom of a pixel,  
 287 and  $t$  is the distance to the top of that pixel. Note that these distances need to have  
 288 been corrected for detector tilt and rotation. Thus the resolution of a pixel in  $Q$  is

$$\Delta Q = \frac{4\pi(\sin \arctan \frac{b}{d} - \sin \arctan \frac{t}{d})}{\lambda} \quad (4.2)$$

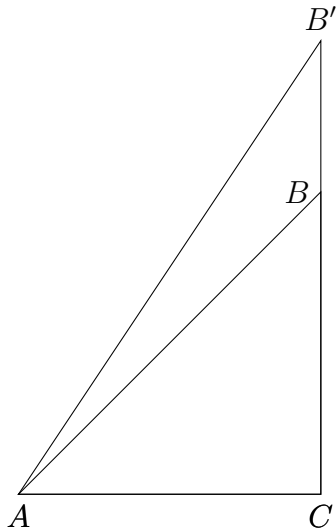


Figure 4.2: Scattering onto a flat detector

289 where  $\lambda$  is the x-ray wavelength.

290 For a Perkin Elmer image plate, like the one used at the NSLS-II's XPD and the  
291 APS's 11-ID-B, the resolution function is shown in 4.3. For the same detector the  
292 number of pixels per  $Q$  is shown in 4.4

## 293 **Automated Mask Generation**

### 294 **Introduction**

295 Detector masking is an important part of any x-ray scattering workflow as dead/hot  
296 pixels, streak errors, and beamstop associated features can be averaged into the data  
297 changing the signal and its statistical significance. While some features, like the  
298 beamstop holder, can be easily observed and masked by hand other are much more  
299 difficult to observe even on large computer monitors. Additionally, while dead/hot  
300 pixels and streaks are usually static the hot pixels associated with textured or sin-  
301 gle crystal scattering or cosmic rays are not. Thus, coming up with an automated  
302 method for finding such erroneous pixels is important, especially as high flux diffrac-  
303 tion beamlines can generate data very quickly.

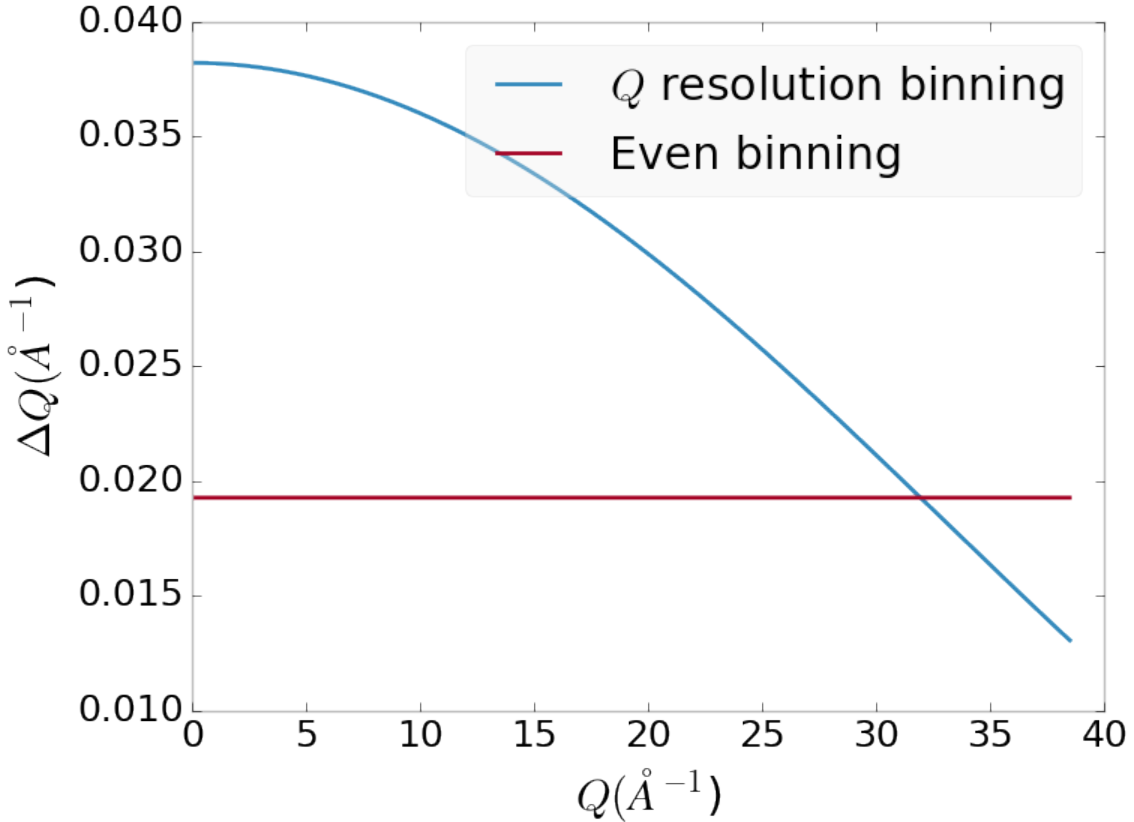


Figure 4.3:  $Q$  resolution as a function of  $Q$ .

304 While this problem can be quite complex in the most general case, we can use the  
 305 annular symmetry of the powder scattering pattern to our advantage, by comparing  
 306 a pixel against pixels in the same ring. Since non-textured powder scattering should  
 307 produce the same pixel intensity for a given ring we can mask any pixels which are  $\alpha$   
 308 standard deviations away from the mean. This method relies on the aforementioned  
 309 pixel binning algorithm, as using miss sized bins will cause some pixels which should  
 310 be in separate rings to be put together, and others which should be in the same ring  
 311 to be separated. In that case the masking algorithm will overestimate the number of  
 312 pixels to be masked due to the additional statistical variation in the sample.

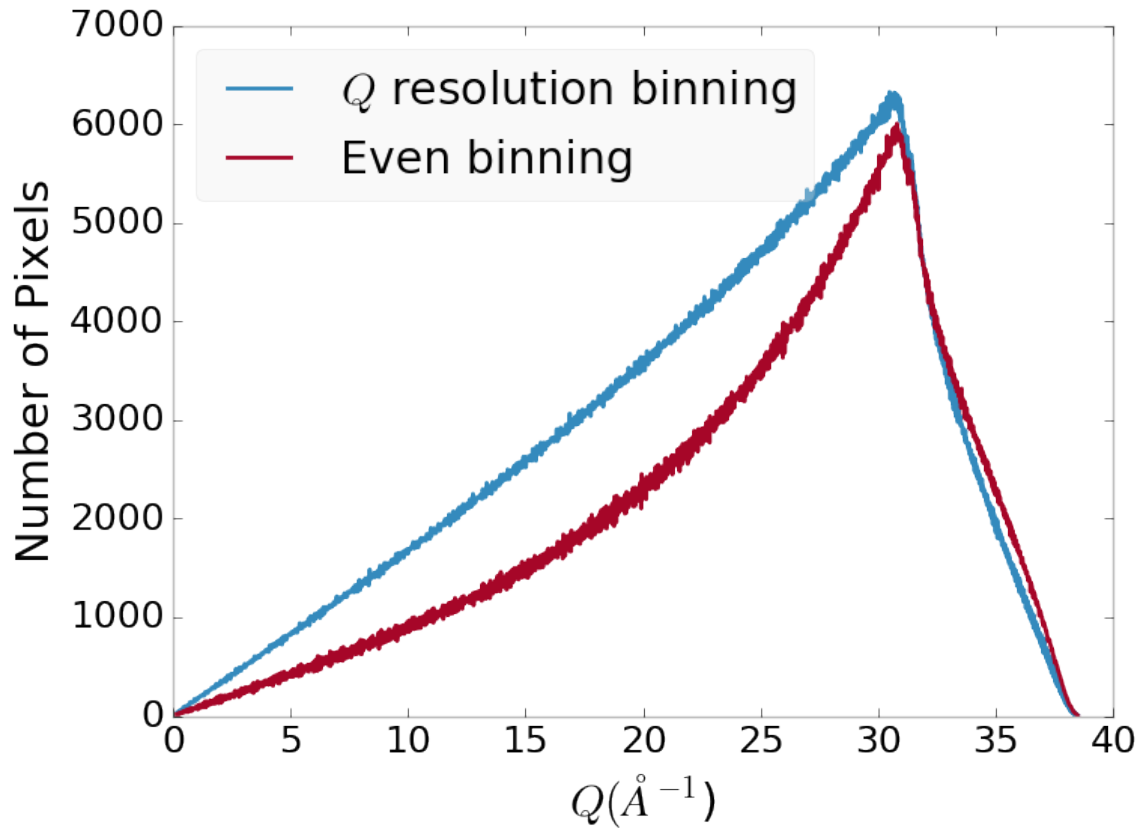


Figure 4.4: Number of pixels as a function of  $Q$ , binned at the  $Q$  resolution of the detector.

### 313 Algorithm Design

314 The masking algorithm procedure takes in the image and a description of the pixel  
 315 positions in either distance from the point of incidence or in  $Q$ . The image is then  
 316 integrated twice, producing both the mean  $I(Q)$  and the standard deviation of each  
 317  $I(Q)$  ring. The mask is created by comparing the pixel values against each ring's  
 318 standard deviation and threshold  $\alpha$ . Note that the threshold can be a function of  
 319 distance from the point of incidence or  $Q$ .

### 320 Test Cases

321 To study the effectiveness of the masking we ran the algorithm against both simulated  
 322 experimental data. In the case of the simulated data four systems were created: 1)

323 dead/hot pixels with varying numbers of defective pixels, 2) beamstop holder with  
324 varying beamstop holder transmittance, 3) rotated beamstop holder with varying  
325 beamstop holder transmittance, and 4) beamstop holder with dead/hot pixels. The  
326 base scattering was produced by

$$I = 100 \cos(50r)^2 + 150 \quad (4.3)$$

327 where  $r$  is a pixel's distance from the beam point of incidence. The positions of  
328 the dead/hot pixels were chosen at random as was the dead or hot nature of the  
329 defect. Dead pixels had values from 0 to 10, while hot pixels had values from 200  
330 to 255. The beamstop was positioned at the vertical center of the detector with an  
331 initial width of 60 pixels and final width of 120 pixels. The hight of the beamstop  
332 was 1024 pixels. The beamstop was calculated to attenuate the x-ray scattering  
333 signal at various transmittance, as various beamstop holder materials have different  
334 transmittance. Two version of the masking algorithm were run for each test case, one  
335 using the standard even bin sizes for the integration step, and one where the bin sizes  
336 are tuned to the pixel  $Q$  resolution as discussed in 4.2.

### 337 **Results and Discussion**

338 Figures 4.5-4.12 show the results of the masking algorithm on simulated images. The  
339 dead/hot pixel masking shows the importance of using the  $Q$  resolution based bin sizes  
340 as the even bin based mask have a tendency to over mask the image, removing pixels  
341 which contain valuable signal. This overmasking is caused by pixels being improperly  
342 associated with one another by the even bins. Figure 4.5 indicates that the masking  
343 algorithm, with the proper binning, masks the image perfectly, with no missed bad  
344 pixels or good pixels masked. This is not the case in figures 4.6 - 4.8 as we can see  
345 pixels which should have been masked but were not. Despite these missed pixels no  
346 pixels were improperly masked in any of the well binned images. These test cases  
347 are actually more difficult than experimental data, as the dynamic range of most

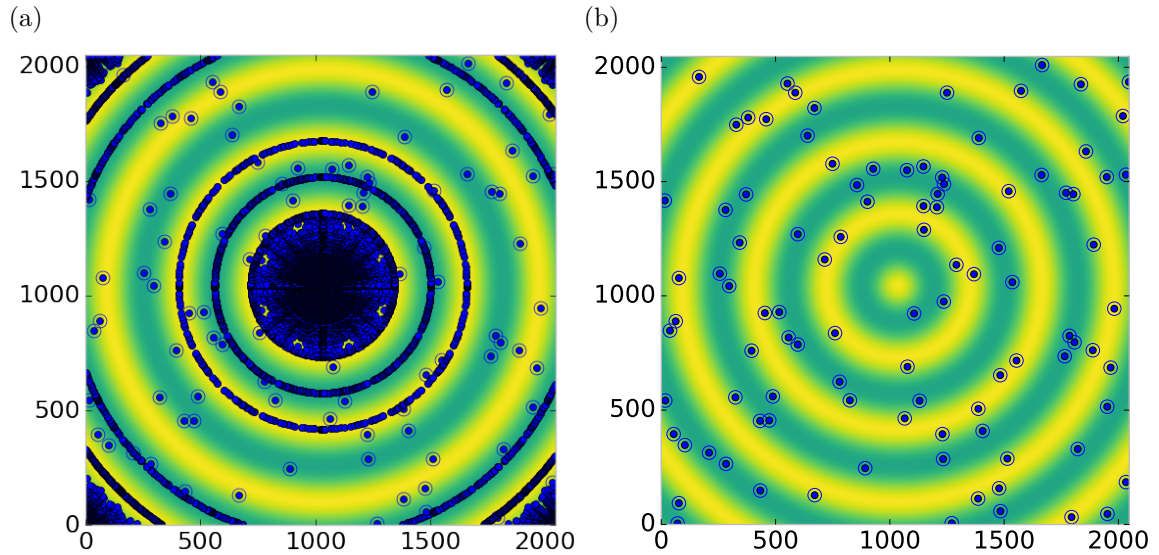


Figure 4.5: Generated dead/hot pixel masks for a detector with 100 bad pixels. a) the standard even bin mask and b) the  $Q$  resolution binned mask. The bad pixels are noted with open circles, masked pixels are noted with closed circles.

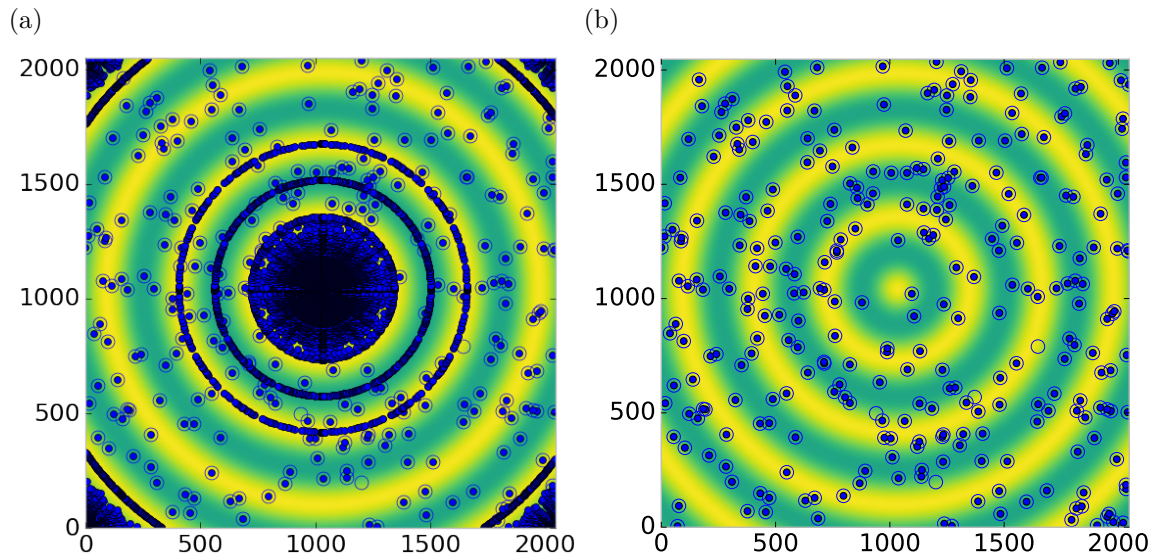


Figure 4.6: Generated dead/hot pixel masks for a detector with 300 bad pixels. a) the standard even bin mask and b) the  $Q$  resolution binned mask. The bad pixels are noted with open circles, masked pixels are noted with closed circles.

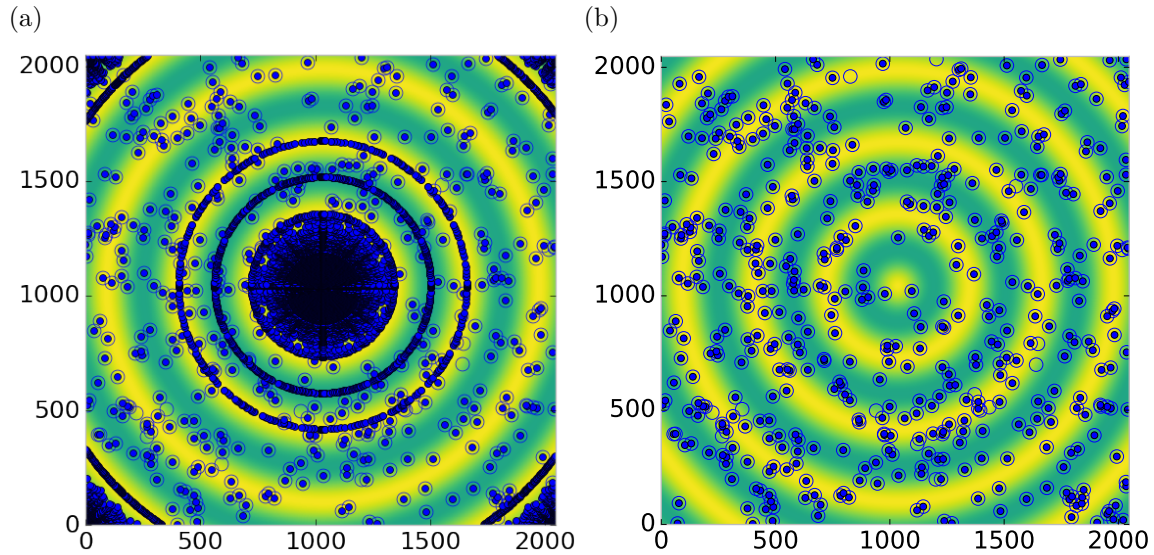


Figure 4.7: Generated dead/hot pixel masks for a detector with 500 bad pixels. a) the standard even bin mask and b) the  $Q$  resolution binned mask. The bad pixels are noted with open circles, masked pixels are noted with closed circles.

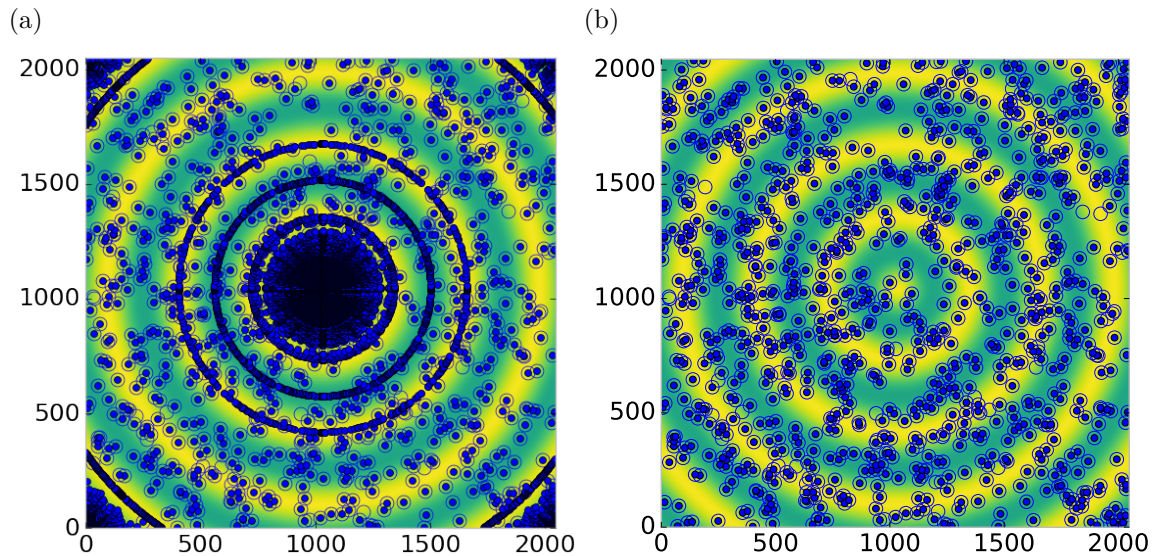


Figure 4.8: Generated dead/hot pixel masks for a detector with 1000 bad pixels. a) the standard even bin mask and b) the  $Q$  resolution binned mask. The bad pixels are noted with open circles, masked pixels are noted with closed circles.

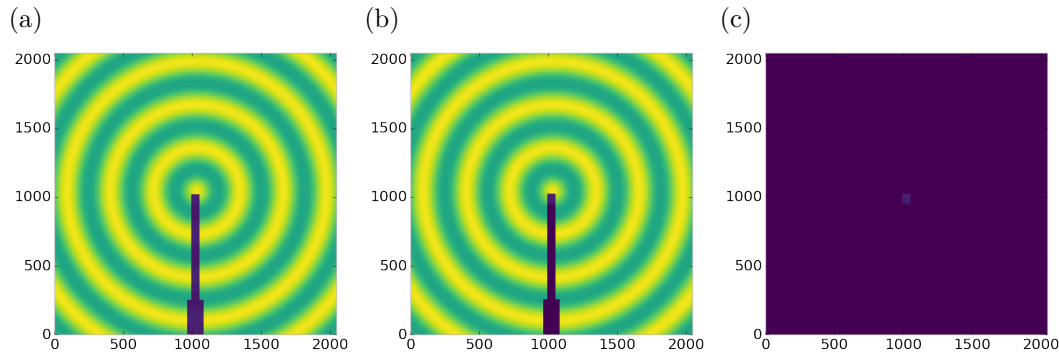


Figure 4.9: Generated beamstop holder masks for a beamstop holder with 10% transmittance. a) the raw image, b) the masked image, c) and the missed pixels

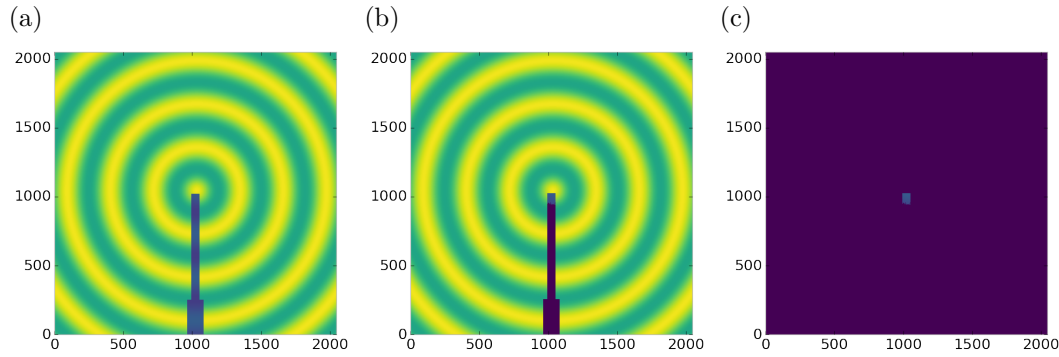


Figure 4.10: Generated beamstop holder masks for a beamstop holder with 30% transmittance. a) the raw image, b) the masked image, c) and the missed pixels

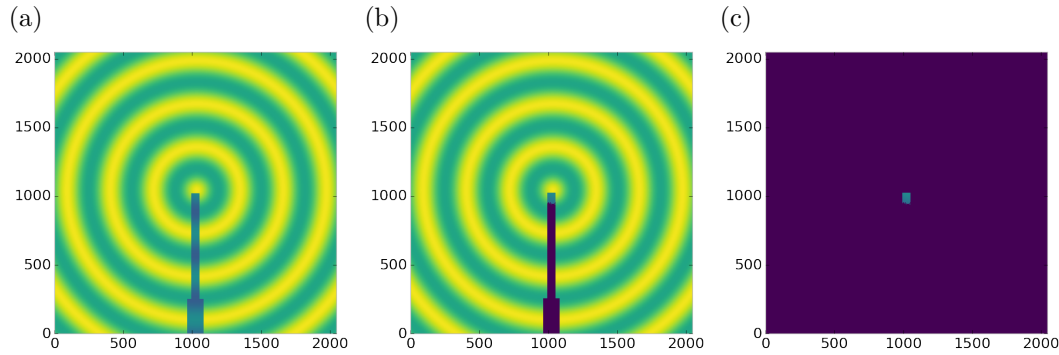


Figure 4.11: Generated beamstop holder masks for a beamstop holder with 50% transmittance. a) the raw image, b) the masked image, c) and the missed pixels

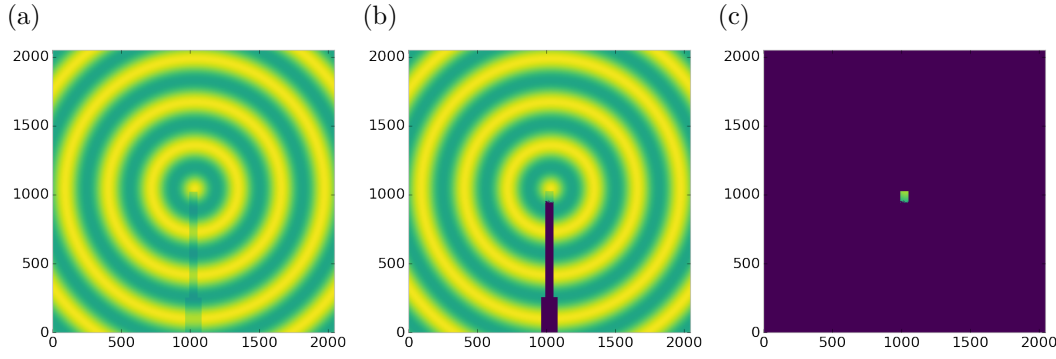


Figure 4.12: Generated beamstop holder masks for a beamstop holder with 90% transmittance. a) the raw image, b) the masked image, c) and the missed pixels

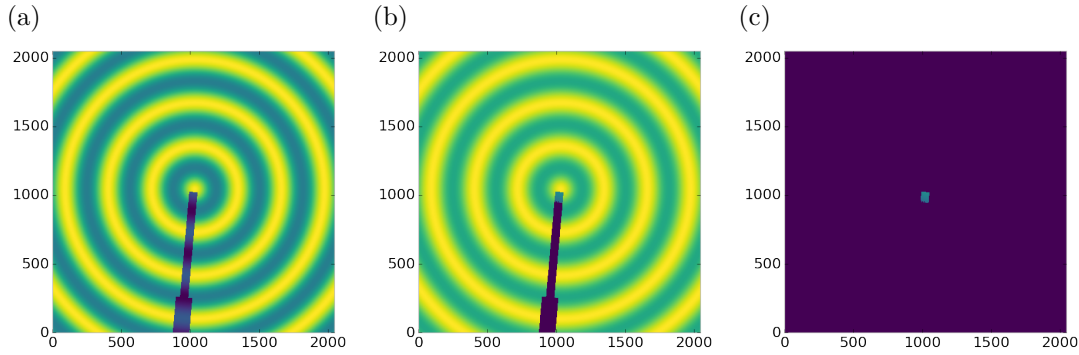


Figure 4.13: Generated beamstop holder masks which is rotated away from verticle

348 detector causes the dead/hot pixels and single crystal/texture peaks to be orders of  
 349 magnitude away from the desired signal.

350 The beamstop holder masks shown in figures 4.9 - 4.12, which were all run with  
 351 the  $Q$  resolution binning show similar results across the transmittance range, missing  
 352 only a small part of the beamstop holder near the point of incidence. Near this point  
 353 the beamstop holder becomes a statisticly significant part of the total number of  
 354 pixels in a given ring, thus it can not be masked out using a statistical search of the  
 355 rings. For most PDF and XRD studies this small area can be masked automaticly  
 356 by masking all the pixels who's distance from the point of incidence is smaller than a  
 357 given radius  $r$ , or can be negelected outright as the area is not used in the analysis or  
 358 refinement. Similar results were produced for beamstop holders which were rotated  
 359 away from the vericle position, as shown in figure 4.13

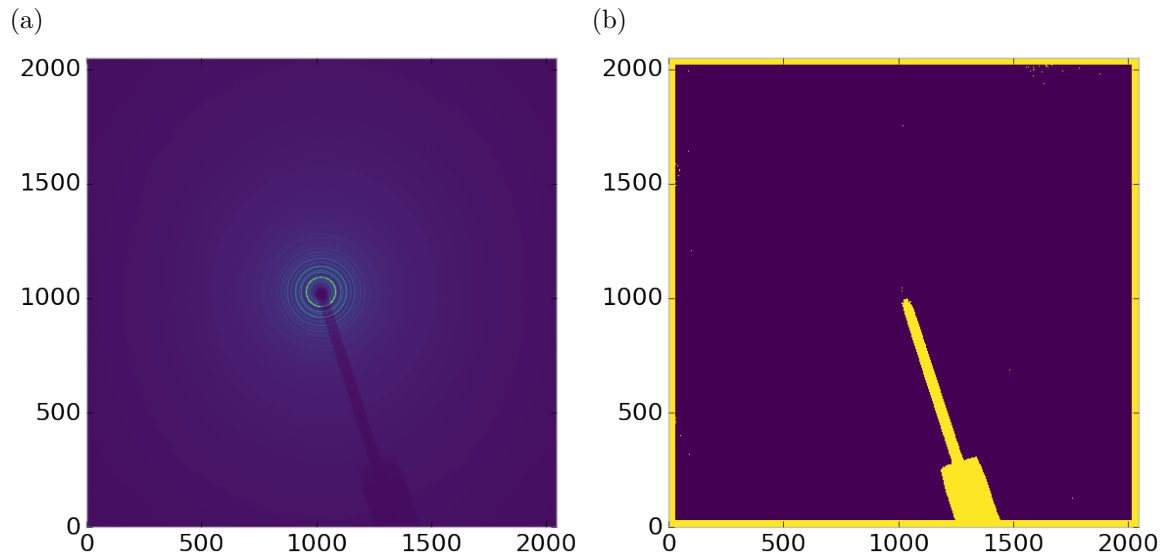


Figure 4.14: Masked experimental data. a) the raw image, b) the mask

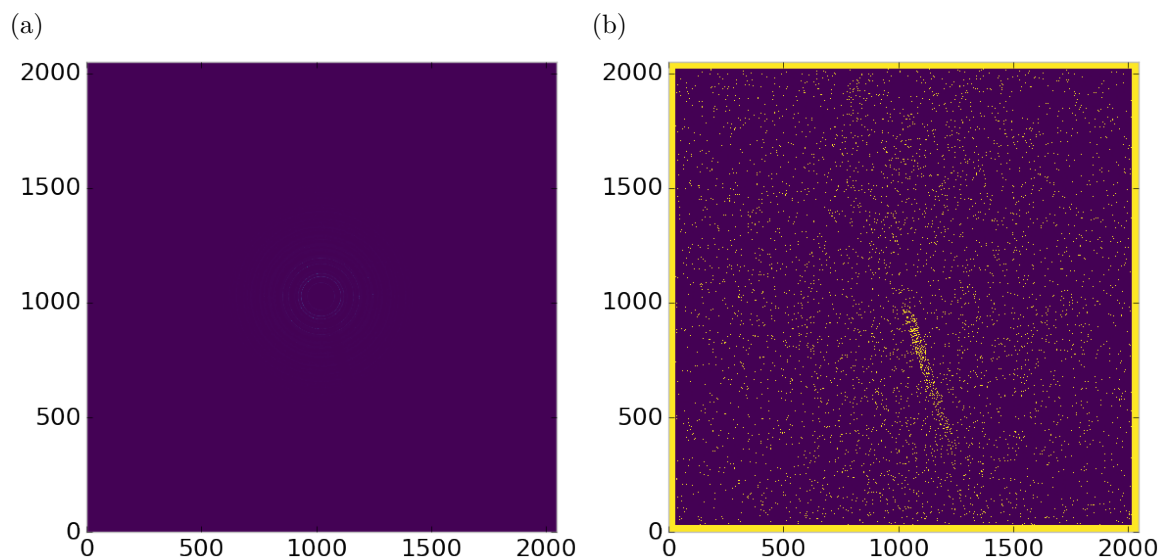


Figure 4.15: Masked experimental data with Pt single crystal signal. a) the raw image, b) the mask

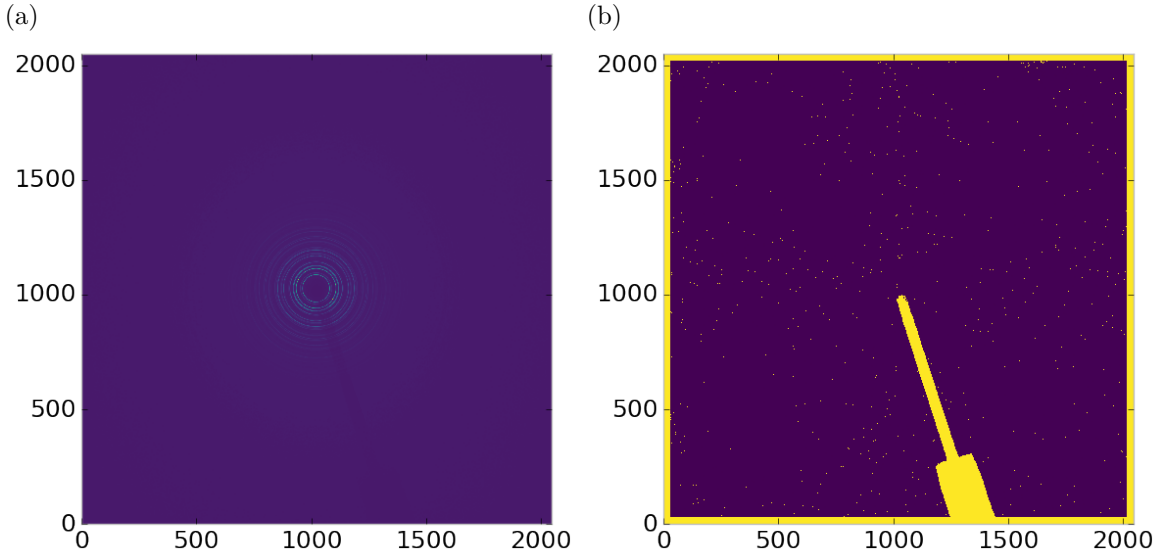


Figure 4.16: Masked experimental data with Pt single crystal signal using figure's 4.14 as a starting mask. a) the raw image, b) the mask

Working with actual experimental data, obtained at the Advanced Photon Source beamline 11-ID-B, shows the difficulty of masking images which have low phonon counts. While the masking of experimental data taken with longer exposures, consisting of 250 .2 second shots, shown in figure 4.14 provides very sharp edges to the beamstop holder, and very little extra masking beyond the occasional dead pixel, this is not the case for the single crystal data. The single crystal data is more problematic because of its short exposure time and low flux, with 500 frame at a .1 second exposure and having shrunk the beam size. The low flux is to prevent the very strong single crystal peaks from damaging the detector. However, this causes the image to be less statistically viable than ideal, causing problems with the mask as seen in figure 4.15. This can be alleviated to some degree by using the previously generated mask as a starting mask for the single crystal image, as shown in 4.16. While the masking algorithm still produces many diffuse masked pixels, they are far fewer, this may be due to the removal of the beamstop which could have contributed to the large standard deviation in figure 4.15.

375 **Conclusions**

376 In this section the masking algorithm, which relies on both  $Q$  resolution based binning  
377 and a statistical approach to azimuthal symmetry, was developed. The focus of  
378 this algorithm was to remove many unwanted detector features associated with pixel  
379 defect, beamstop holder associated scattering attenuation, and single crystal/texture  
380 peaks. Simulated data was used to evaluate the beamstop holder and dead/hot pixel  
381 masking capacity, while experimental data was used to check for single crystal and  
382 texture based masking.  $Q$  resolution based binning was shown to be very important to  
383 avoid overmasking. The ability of the mask writer to mask images is somewhat limited  
384 by the overall statistical image quality, although some deficiencies can be obtained by  
385 using previously generated masks as starting points. This masking algorithm is now  
386 in use in the data processing workflow and will be available in scikit-beam soon.

387 **Automated Image Azimuthal Integration**

388 Using the  $Q$  resolution binning and masking developed in sections 4.2 and 4.2 the  
389 images can be properly integrated. Generally, images are integrated by taking the  
390 mean value of the pixels in a ring. However, other statistical measures of the average  
391 value can be used, like the median.

392 Figures 4.17-4.19 show the importance of masking and the choice of average func-  
393 tion. All the figures were produced using the same dataset, 50 °C  $\text{Pr}_2\text{NiO}_4$  taken at  
394 the APS's 11-ID-B on a Perkin Elmer area detector. The automatic masking alpha  
395 was 3 standard deviations from the mean. While it is difficult to observe the changes  
396 the mask causes in the full  $I(Q)$  plot (subfigures a) and b)), the standard deviation  
397 plots show the effect of bad pixels on the data (subfigure c)). Subfigure c) for figures  
398 4.17-4.19 shows that removal of the beamstop holder lowers the low  $Q$  standard de-  
399 viation from around .1 to almost .01 out to 15  $\text{\AA}^{-1}$ . The high  $Q$  subfigures d) and f)  
400 in figures 4.17-4.19 show the “kink” effect of the detector edge and beamstop holder,

401 where there is a dip in the  $I(Q)$  scattering when the rings include the edge of the  
402 detector. This effect seems to be due to both errors in the edge pixel intensity and the  
403 beamstop holder as masking of the edges only seems to provide only partial removal  
404 of the issue. It is important to note that while integration using the mean of the  
405 ring has issues with only the edge mask, as evidenced by the change in slope in 4.18  
406 d) around  $29.5 \text{ \AA}^{-1}$ , the median integration does not include this error. Ideally the  
407 detector would have a normal distribution of pixel intensity for a given ring, which  
408 would imply an equivalency between the mean and median  $I(Q)$  values. Despite the  
409 closeness of the mean and median once the final mask has been created, it seems that  
410 the median is more reliable, as it was less effected by the beamstop holder in figure  
411 4.18. Thus, for subsequent integrations discussed in this work the median is used to  
412 avoid any defective features that the masking algorithm may have missed.

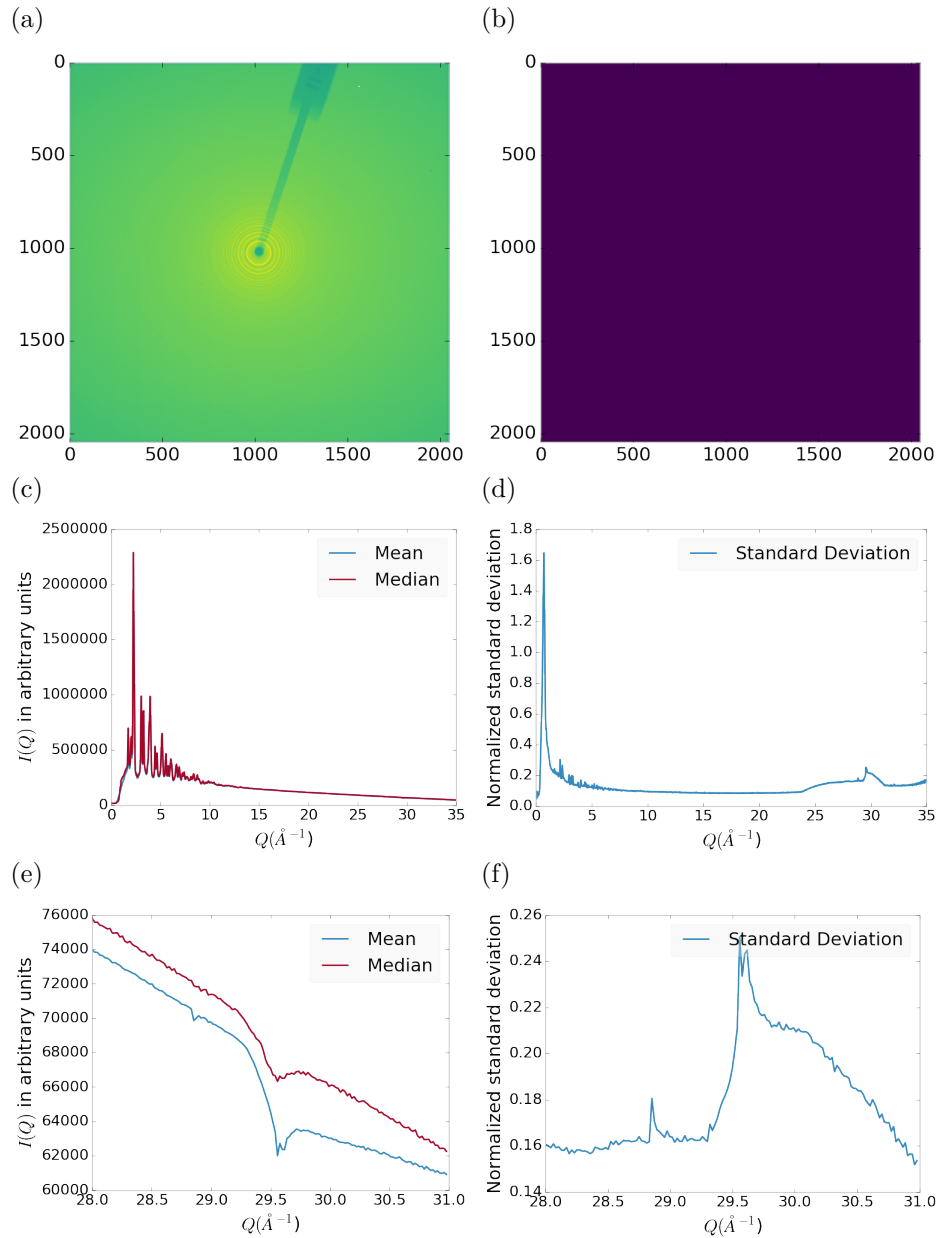


Figure 4.17: Masking, average, and standard deviation of an example x-ray total scattering measurement. This image was produced with no mask. a) the image, b) the mask, c) the mean and median values, d) the standard deviation (normalized to the median), e) a closeup of the  $28 \text{ \AA}^{-1}$  to  $31 \text{ \AA}^{-1}$   $Q$  range for the mean and median, f)  $28 \text{ \AA}^{-1}$  to  $31 \text{ \AA}^{-1}$   $Q$  range for the standard deviation

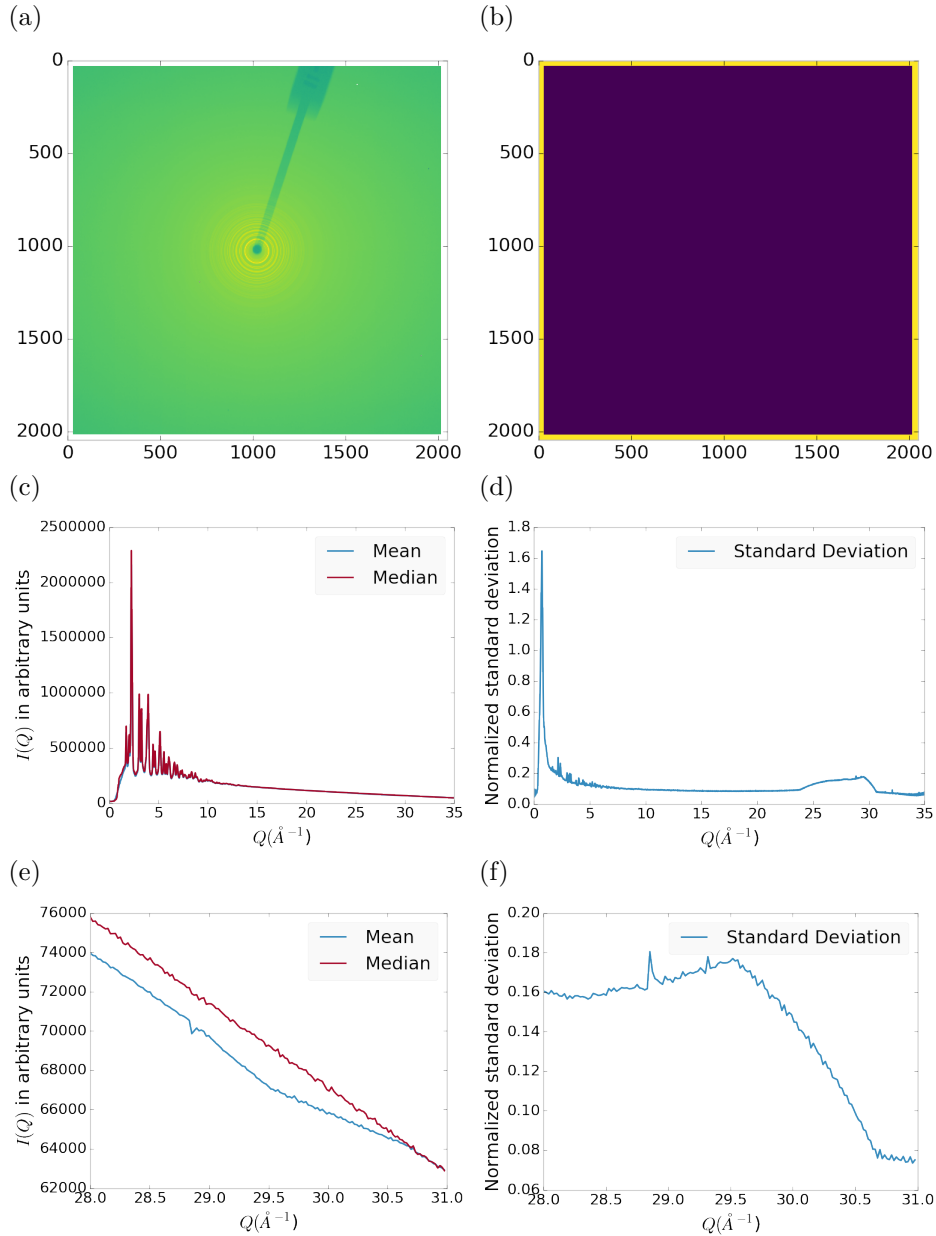


Figure 4.18: Masking, average, and standard deviation of an example x-ray total scattering measurement. This image was produced with only an edge mask. a) the image, b) the mask, c) the mean and median values, d) the standard deviation (normalized to the median), e) a closeup of the  $28 \text{ \AA}^{-1}$  to  $31 \text{ \AA}^{-1}$   $Q$  range for the mean and median, f)  $28 \text{ \AA}^{-1}$  to  $31 \text{ \AA}^{-1}$   $Q$  range for the standard deviation

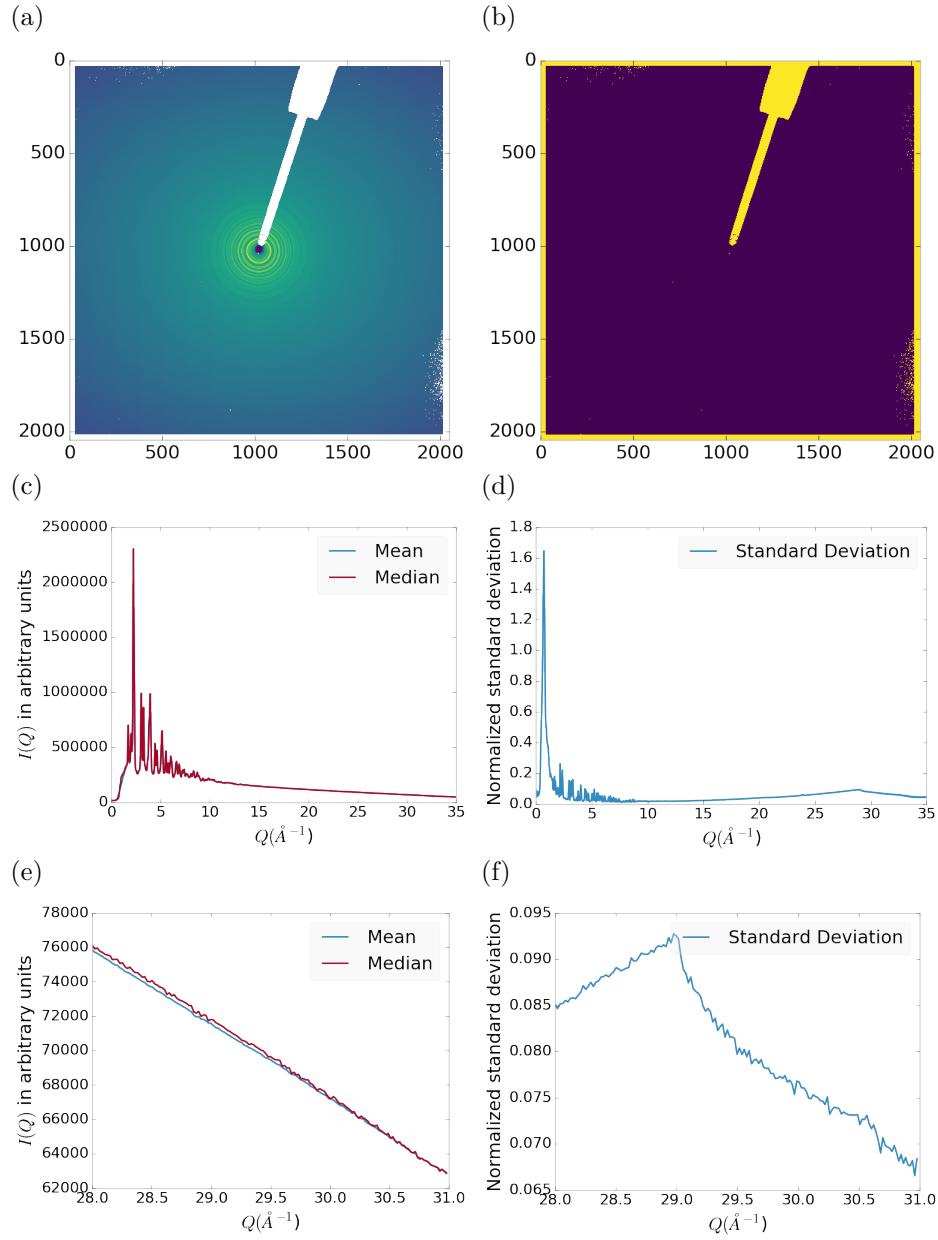


Figure 4.19: Masking, average, and standard deviation of an example x-ray total scattering measurement. This image was produced combining an edge mask and the automatically generated mask. a) the image, b) the mask, c) the mean and median values, d) the standard deviation (normalized to the median), e) a closeup of the  $28 \text{ \AA}^{-1}$  to  $31 \text{ \AA}^{-1}$   $Q$  range for the mean and median, f)  $28 \text{ \AA}^{-1}$  to  $31 \text{ \AA}^{-1}$   $Q$  range for the standard deviation

413

## CHAPTER 5

414

### ANNEALING AND AGGREGATION OF 2NM

415

#### AU NANOPARTICLES

416 5.1 EXPERIMENTS

417 NP Synthesis

418 X-ray Total Scattering Measurements

419 5.2 DATA PROCESSING

420 5.3 DATA ANALYSIS

421 5.4 SIMULATION

422 5.5 STRUCTURAL ANALYSIS

423 5.6 CONCLUSIONS

424

## CHAPTER 6

425

### PHASE CHANGES AND ANNEALING DYNAMICS OF

426

### $\text{Pr}_2\text{NiO}_4$ AND ITS DERIVATIVES

427

#### 6.1 EXPERIMENTS

428

##### $\text{Pr}_2\text{NiO}_4$ Synthesis

429

##### X-ray Total Scattering Measurements

430

##### DATA PROCESSING

431

##### DATA ANALYSIS

432

##### Intra Sample Comparison

433

##### Inter Sample Comparison

434

##### SIMULATION

435

##### Small Box

436

##### Large Box

437

##### STRUCTURAL ANALYSIS

438

##### CONCLUSIONS

439

## CHAPTER 7

440

## CONCLUSION